

MEDIUM-RESOLUTION OPTICAL AND NEAR-INFRARED SPECTRAL ATLAS OF 16 2MASS-SELECTED NIR-RED ACTIVE GALACTIC NUCLEI AT $Z \sim 0.3$

Dohyeong Kim^{1,2}, Myungshin Im^{1,2}, Gabriela Canalizo³, Minjin Kim⁴, Ji Hoon Kim⁵, Jong-Hak Woo², Yoon Chan Taak^{1,2}, Jae-Woo Kim⁴, AND Mariana Lazarova^{6,7}

Draft version December 19, 2018

ABSTRACT

We present medium-resolution spectra ($R \sim 2000\text{--}4000$) at $0.4\text{--}1.0\ \mu\text{m}$ and $0.7\text{--}2.5\ \mu\text{m}$ of 16 active galactic nuclei (AGNs) selected with red color in the near-infrared (NIR) of $J-K > 2.0$ mag at $z \sim 0.3$. We fit the $H\beta$, $H\alpha$, $P\beta$, and $P\alpha$ lines from these spectra to obtain their luminosities and line widths. We derive the $E(B-V)$ color excess values of the NIR-red AGNs using two methods, one based on the line-luminosity ratios and another based on the continuum slopes. The two $E(B-V)$ values agree with each other at rms dispersion ~ 0.249 . About half of the NIR-red AGNs have $g' - K < 5$ magnitude, and we find that these NIR red, but blue in optical-NIR AGNs, have $E(B-V) \sim 0$, suggesting that a significant fraction of the NIR color-selected red AGNs are unobscured or only mildly obscured. After correcting for the dust extinction, we estimate the black hole (BH) masses and the bolometric luminosities of the NIR-red AGNs using the Paschen lines to calculate their Eddington ratios (λ_{Edd}). The median Eddington ratios of nine NIR-red AGNs ($\log(\lambda_{\text{Edd}}) \simeq -0.654 \pm 0.176$) are only mildly higher than those of unobscured type 1 AGNs ($\log(\lambda_{\text{Edd}}) \simeq -0.961 \pm 0.008$). Moreover, we find that the $M_{\text{BH}}\text{--}\sigma_*$ relation for three NIR-red AGNs is consistent with that of unobscured type 1 AGNs at similar redshift. These results suggest that the NIR red color selection alone is not effective at picking up dusty, intermediate-stage AGNs.

Subject headings:

1. INTRODUCTION

In recent years, there has been increased interest in the role of supermassive black holes (SMBHs) in galaxy formation and evolution. Most massive spheroidal galaxies are believed to harbor SMBHs at their centers, and the masses of the SMBHs have a correlation with the luminosities (Magorrian et al. 1998; Bentz et al. 2009; Bennert et al. 2010; Greene et al. 2010; Jiang et al. 2011; Park et al. 2015), the stellar velocity dispersions (Ferrarese & Merritt 2000; Gebhardt et al. 2000; Tremaine et al. 2002; Gültekin et al. 2009; Woo et al. 2010), and Sersic indices (Graham et al. 2001; Graham & Driver 2007) of their spheroids.

The proposed scenario for the growth of SMBHs is that they are assembled by gas accretion (Lynden-Bell 1969). The SMBHs are thought to grow very rapidly in an active phase, i.e., the period of active galactic nuclei (AGNs). During this phase, AGNs emit enormous

amounts of energy ($10^{43}\text{--}10^{48}\text{ erg s}^{-1}$; e.g., Woo & Urry 2002) from gamma-ray to radio. Most of our knowledge of AGNs comes from unobscured type 1 AGNs, found by using surveys of X-ray, ultraviolet (UV), optical, and radio observations (Grazian et al. 2000; Becker et al. 2001; Anderson et al. 2003; Croom et al. 2004; Risaliti & Elvis 2005; Schneider et al. 2005; Véron-Cetty & Véron 2006; Young et al. 2009).

However, several studies (e.g., Comastri et al. 2001; Tozzi et al. 2006; Polletta et al. 2008) have reported that the soft X-ray, UV, and optical based AGN surveys could neglect a large number (e.g., up to more than 50%) of AGNs with very red colors, due to the dust extinction from the intervening dust and gas in their host galaxies (Webster et al. 1995; Cutri et al. 2002). From a similar but different point of view, there is another missing population of AGNs with red colors due to the interstellar medium in our galaxy (Im et al. 2007; Lee et al. 2008).

The AGNs with red colors are called red AGNs, and they are considered to be a different population from unobscured type 1 AGNs. In several simulation studies (Hopkins et al. 2005, 2006, 2008), red AGNs have been predicted to be in an intermediate phase between the merger-driven star-forming galaxies, such as ultra-luminous infrared galaxies (ULIRGs; Sanders et al. 1988; Sanders & Mirabel 1996), and unobscured type 1 AGNs. Although this explanation for red AGNs is still controversial due to several reasons (e.g., Puchnarewicz & Mason 1998; Whiting et al. 2001; Wilkes et al. 2002; Schawinski et al. 2011, 2012; Simmons et al. 2012; Kocevski et al. 2012; Rose et al. 2013), this scenario is further supported by several observational studies. For example, red AGNs have (i) high accretion rates (Urrutia et al. 2012; Kim et al. 2015b), (ii) enhanced star formation activity (Georgakakis et al. 2009), (iii) a frequent occurrence of merging

Electronic address: dohyeong@astro.snu.ac.kr; mim@astro.snu.ac.kr

¹ Center for the Exploration of the Origin of the Universe (CEO), Astronomy Program, Department of Physics and Astronomy, Seoul National University, 1 Gwanak-ro, Gwanak-gu, Seoul 151-742, South Korea

² Astronomy Program, Department of Physics and Astronomy, Seoul National University, 1 Gwanak-ro, Gwanak-gu, Seoul 151-742, South Korea

³ Department of Physics and Astronomy, University of California, Riverside, CA 92521, USA

⁴ Korea Astronomy and Space Science Institute, Daejeon 305-348, South Korea

⁵ Subaru Telescope, National Astronomical Observatory of Japan, 650 North Aohoku Place, Hilo, HI 96720, USA

⁶ Department of Physics and Astronomy, University of Nebraska - Kearney, 2401 11th Avenue, Kearney, NE 68849, USA

⁷ Department of Physics and Astronomy, University of Northern Colorado, Greeley, CO 80639, USA

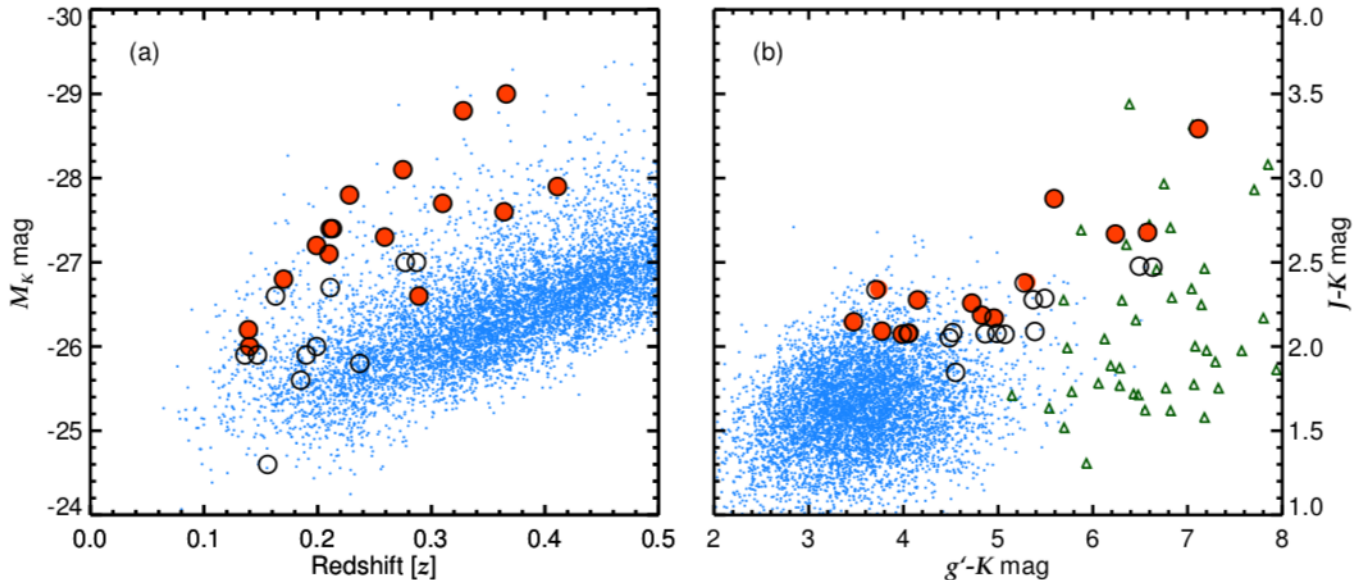


FIG. 1.— (a) Redshifts vs. M_K magnitudes for NIR-red AGNs and unobscured type 1 quasars. The circles represent 29 NIR-red AGNs listed in Marble et al. (2003) and the red filled circles denote 16 NIR-red AGNs used in this work. The blue dots represent the redshifts and M_K magnitudes of unobscured type 1 quasars listed in SDSS DR7 (Shen et al. 2011). (b) Color-color diagram using $g' - K$ and $J - K$ magnitudes. The meanings of the circles and the blue dots are identical to the left panel, and the green triangles denote the $g' - K$ and $J - K$ magnitudes of red quasars used in our previous studies (Kim et al. 2015b; Kim & Im 2018). Here, g' -, J -, and K -band magnitudes are corrected for the Galactic extinction (Schlafly & Finkbeiner 2011), and the g' -band magnitude is in AB unit, while J - and K -band magnitudes are based on the Vega magnitudes.

features (Urrutia et al. 2008; Glikman et al. 2015), (iv) young radio jets (Georgakakis et al. 2012), (v) red continua from dust extinction (Glikman et al. 2007; Urrutia et al. 2009), and (vi) line-luminosity ratios explainable only when considering dust extinction (Kim & Im 2018).

Since the observational results of red AGNs could arise from the limited sample size of red AGNs, there have been several efforts to search for more red AGNs (Webster et al. 1995; Benn et al. 1998; Cutri et al. 2001, 2002; Smith et al. 2002; Glikman et al. 2007, 2012; Urrutia et al. 2009; Banerji et al. 2012; Stern et al. 2012; Assef et al. 2013; Fynbo et al. 2013; Lacy et al. 2013). A significant number of these studies found red AGNs using large-area NIR photometric surveys, such as the Two Micron All-Sky Survey (2MASS; Skrutskie et al. 2006), the UKIRT Infrared Deep Sky Survey (UKIDSS; Lawrence et al. 2007), and the *Wide-field Infrared Survey Explorer* (*WISE*; Wright et al. 2010) survey.

Compared to how large-area NIR photometric surveys have contributed to our understanding of red AGNs, investigations based on NIR spectroscopic data (e.g., Glikman et al. 2007, 2012; Kim et al. 2015b) are limited. Despite the limited contribution, the NIR spectrum includes useful information for investigating the nature of red AGNs. For example, (i) BH masses (Paschen lines: Kim et al. 2010; Landt et al. 2011b, and Brackett lines: Kim et al. 2015a), (ii) bolometric luminosities (Kim et al. 2010), (iii) broad-line region (BLR) sizes (Landt et al. 2011a), (iv) temperatures (Glikman et al. 2006; Landt et al. 2011b; Kim et al. 2015a) and covering factors of hot dust (Kim et al. 2015a), (v) stellar velocity dispersions (σ_* ; Woo et al. 2010; Kang et al. 2013), and (vi) star forming activity (Imanishi et al. 2011; Kim et al. 2012) can be measured from the NIR spectra.

In this work, we present high signal-to-noise ratio

(S/N; up to several hundreds) and medium-resolution ($R \sim 2000$) optical and NIR spectra of a sample of 16 NIR-red AGNs at $z \sim 0.3$, for which optical images and polarizations were obtained in previous studies (Smith et al. 2002; Marble et al. 2003). We concentrate on a detailed description of our sample and observation (§ 2), spectral fittings for hydrogen lines (§ 3), dust-reddening measurements (§ 4), accretion rates (§ 5), and the $M_{\text{BH}} - \sigma_*$ relation for NIR-red AGNs (§ 6). In § 7, we briefly summarize our results. Throughout this work, we use a standard Λ CDM cosmological model of $H_0 = 70 \text{ km s}^{-1} \text{ Mpc}^{-1}$, $\Omega_m = 0.3$, and $\Omega_\Lambda = 0.7$, supported by past observational studies (e.g., Im et al. 1997). Our photometry uses the Vega magnitude system, except for the g' band that is in the AB system.

2. THE SAMPLE AND OBSERVATION

2.1. Sample

Our sample is drawn from the 29 2MASS-based red AGNs listed in Marble et al. (2003). The 29 objects were selected with the following procedures. First, Cutri et al. (2001, 2002) chose red AGN candidates through a combination of red color in NIR ($J - K_s > 2$) and detection in each of the three 2MASS bands (complete to $K_s < 15.0 \text{ mag}$). Then, among the candidates, 70 targets were spectroscopically confirmed in Smith et al. (2002). Furthermore, Smith et al. (2002) performed optical polarimetric observations using the Two-Holer Polarimeter/Photometer on the Steward Observatory 1.5 m telescope and the Bok 2.3 m reflector. Finally, Marble et al. (2003) selected 29 out of the 70 NIR-red AGNs within the redshift range of $0.136 \leq z \leq 0.596$, and observed them with the Wide Field Planetary Camera 2 (WFPC2) on board the *Hubble Space Telescope* (*HST*).

Among the 29 NIR-red AGNs, we select 16 AGNs at

TABLE 1
OBSERVING SUMMARY

Object	R.A. (J2000.0)	Decl. (J2000.0)	Redshift (z)	K_s (mag)	M_{K_s} ^a (mag)	NIR Spectroscopy			Optical Spectroscopy		
						Telescope/ Instrument	Exp (s)	Observing dates	Telescope/ Instrument	Exp (s)	Observing dates
0106+2603	01 06 07.7	+26 03 34	0.411	14.6	-27.9	Subaru/IRCS	800 ^b 6000 ^c	2015 Nov 2015 Nov	Keck/ESI	3600	2003 Oct
0157+1712	01 57 21.0	+17 12 48	0.213	13.2	-27.4	Gemini/GNIRS	3600	2015 Aug	Keck/ESI	7200	2003 Oct
0221+1327	02 21 50.6	+13 27 41	0.140	13.2	-26.0	Magellan/FIRE	6657	2015 Jan	Keck/ESI	5400	2003 Oct
0234+2438	02 34 30.6	+24 38 35	0.310	13.7	-27.7	Gemini/GNIRS	2160	2015 Aug	—	—	—
0324+1748	03 24 58.2	+17 48 49	0.328	12.8	-28.8	Magellan/FIRE	3635	2015 Jan	Keck/ESI	3600	2004 Sep
0348+1255	03 48 57.6	+12 55 47	0.210	13.6	-27.1	Gemini/GNIRS	2880	2015 Aug	Keck/ESI	3600	2004 Sep
1258+2329	12 58 07.4	+23 29 21	0.259	13.4	-27.3	IRTF/Spex	9000	2016 Mar	SDSS	—	—
1307+2338	13 07 00.6	+23 38 05	0.275	13.4	-28.1	IRTF/Spex	18000	2016 Mar	—	—	—
1453+1353	14 53 31.5	+13 53 58	0.139	13.1	-26.2	IRTF/Spex	9600	2016 Mar	SDSS	—	—
1543+1937	15 43 07.7	+19 37 51	0.228	12.7	-27.8	Gemini/GNIRS	3600	2016 Apr	Keck/ESI	3600	2004 Jul
						IRTF/Spex	9600	2016 Mar	—	—	—
1659+1834	16 59 39.7	+18 34 36	0.170	12.9	-26.8	IRTF/Spex	8400	2016 Mar	Keck/ESI	5400	2004 Jul
2222+1952	22 22 02.2	+19 52 31	0.366	13.3	-29.0	Gemini/GNIRS	2160	2015 Aug	—	—	—
2222+1959	22 22 21.1	+19 59 47	0.211	12.9	-27.4	Gemini/GNIRS	2880	2015 Aug	Keck/ESI	5400	2004 Sep
2303+1624	23 03 04.3	+16 24 40	0.289	14.7	-26.6	Gemini/GNIRS	5040	2015 Aug	—	—	—
2327+1624	23 27 45.6	+16 24 34	0.364	14.5	-27.6	Gemini/GNIRS	3600	2015 Aug	Keck/ESI	5400	2004 Sep
2344+1221	23 44 49.5	+12 21 43	0.199	12.9	-27.2	Gemini/GNIRS	2880	2015 Aug	Keck/ESI	3600	2004 Jul

^a The M_{K_s} values are recalculated using the method of Marble et al. (2003) with the standard Λ CDM cosmological model

^b The grism mode observation

^c The echelle mode observation

$z \sim 0.3$ (from 0.139 to 0.411) for which the redshifted $P\beta$ or $P\alpha$ line is observable within the sky window wavelength range. The 16 NIR-red AGNs span over a wide range of luminosities ($-29.0 < M_K < -26.0$). Figure 1 shows the redshifts versus the M_K magnitudes and $g' - K$ colors versus the $J - K$ colors of the 16 NIR-red AGNs and red quasars used in our previous studies (Kim et al. 2015b; Kim & Im 2018; originally from Urrutia et al. 2009). These NIR-red AGNs have red colors of $J - K > 2$ and $g' - K \gtrsim 4$. Compared to the red quasars that we studied previously ($J - K > 1.3$ and $g' - K > 5$), a non-negligible fraction of the 16 NIR-red AGNs possess $g' - K < 5$ as blue as those of unobscured type 1 quasars.

For our sample, we emphasize the advantage of the availability of various types of high-quality data. The 16 NIR-red AGNs have optical images from *HST* (Marble et al. 2003) and optical broadband polarimetry (Smith et al. 2002). We expect that a combined data set of the high-quality images from the *HST* data, the optical polarization, and the optical/NIR spectra from this study will be unique and useful for the comprehensive investigations of the nature of NIR-red AGNs.

2.2. NIR Observation

We performed NIR spectroscopic observations with four telescopes and their respective instruments. Since the 16 NIR-red AGNs have different brightnesses and redshifts, the observations need to be performed with proper observational instruments and telescopes to fit the characteristics of the 16 NIR-red AGNs. We describe the details of our NIR observations below.

First, NIR spectra of nine NIR-red AGNs were obtained with the cross-dispersed mode of the Gemini Near-infrared Spectrograph (GNIRS; Elias et al. 2006) on the 8.1 m Gemini-North telescope. The observational configuration is a combination of a 110 l/mm grating, short blue camera, and $0''.675$ slit width, which provides a discontinuous spectral coverage from $\sim 1 \mu\text{m}$ to $\sim 2.1 \mu\text{m}$

with a spectral resolution of $R \sim 2600$.

Second, we used the SpeX (Rayner et al. 2003) on the 3.0 m NASA Infrared Telescope Facility (IRTF) for five NIR-red AGNs. In this observation, we used the short cross-dispersion mode (SXD) with a $0''.3$ slit width to achieve a spectral resolution of $R \sim 2000$ across $0.7 - 2.55 \mu\text{m}$. Among these five NIR-red AGNs, one, 1543+1937, overlaps with the nine NIR-red AGNs observed with GNIRS/Gemini.

Third, in order to obtain the NIR spectra of two NIR-red AGNs, we used the Folded-port Infrared Echellette (FIRE) on the 6.5 m Magellan Baade telescope with a $1''.0$ slit width. This observational configuration allows the wavelength coverage to span from 0.82 to $2.51 \mu\text{m}$ with a resolving power of $R \sim 3600$.

Fourth, an NIR spectrum of one NIR-red AGN was obtained with the Infrared Camera and Spectrograph (IRCS; Tokunaga et al. 1998; Kobayashi et al. 2000) on the 8.2 m Subaru telescope. In this observation, we used both grism and echelle modes. For the grism mode observation, we used a $0''.1$ slit width and HK band with the grism of 52 milliarsecond pixel scale, which provides a spectral coverage of $1.4 - 2.5 \mu\text{m}$ with a spectral resolution of $R \sim 440$. The Echelle mode observation was performed with a $0''.54$ slit width and K band, and this provides a spectral resolution of $R \sim 6600$ with a discontinuous wavelength coverage from $1.90 \mu\text{m}$ to $2.49 \mu\text{m}$.

Our observations were performed under clear weather conditions with sub-arcsecond seeings of $\sim 0''.6$. For the flux calibration and telluric correction, we observed nearby AOV stars before or after the observations of the NIR-red AGNs. In order to produce fully reduced spectra, we used Gemini image reduction and analysis facility packages (Cooke & Rodgers 2005), Spextool (Vacca et al. 2003; Cushing et al. 2004), FIREHOSE, and general reduction procedure of spectra with image reduction and analysis facility (Massey et al. 1988) for the spectra obtained with GNIRS, SpeX, FIRE, and IRCS, respec-

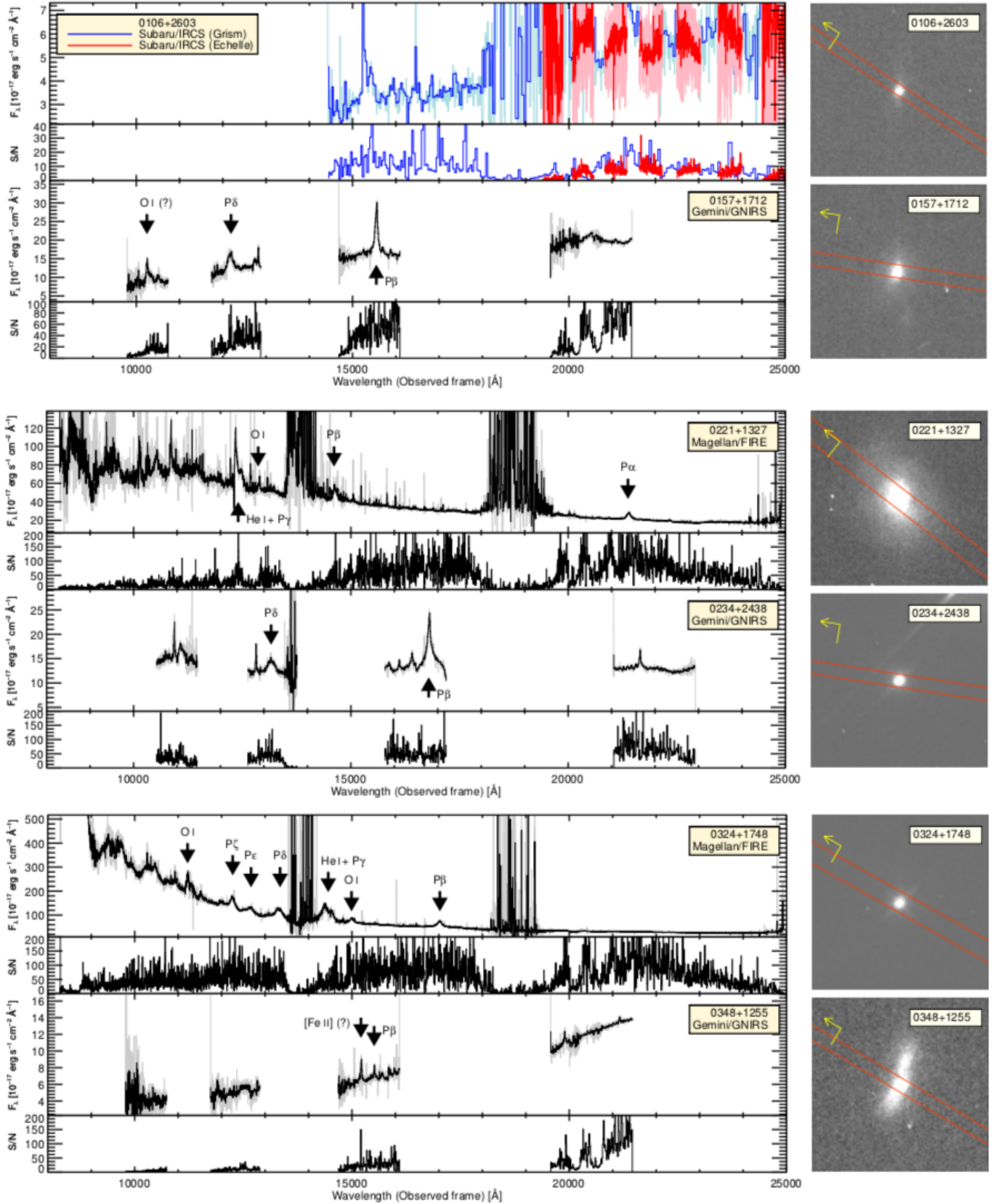


FIG. 2.— (Left) NIR spectra of 16 NIR-red AGNs and their S/Ns. The gray lines indicate observed spectra in the observed frame, and the black lines indicate binned spectra with the spectral resolution. For 0106+2603 and 1543+1937, the spectra were obtained with two different observing modes and instruments. Each binned spectrum from an individual observation is represented by the blue and red lines, and the sky blue and pink lines indicate their original spectra, respectively. Moreover, several emission lines (P α : 1.8751 μm , P β : 1.2818 μm , P γ : 1.0938 μm , P δ : 1.0049 μm , P ϵ : 0.9546 μm , P ζ : 0.9229 μm , [Fe II]: 1.5995 and 1.2567 μm , O I: 1.1287, and 0.8446 μm , and He I: 1.0830 μm) are marked on the spectra. However, when the emission line is not obvious due to the low S/N or duplicate sky lines, the emission line is marked with a question mark. (Right) *HST* images of 16 NIR-red AGNs. The red boxes across the objects indicate slit widths and the yellow arrows at the top left denote north.

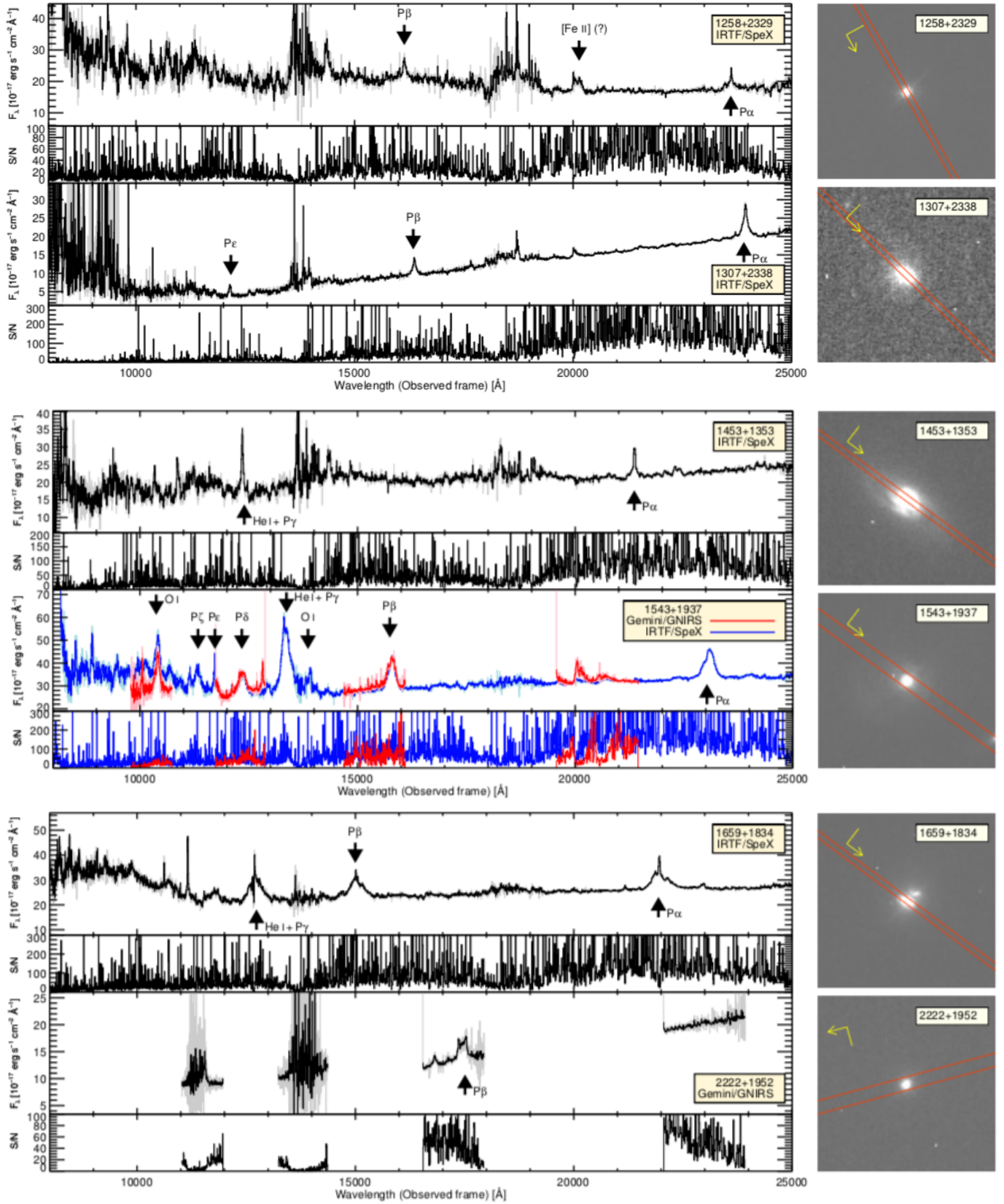


FIG. 2.— Continued

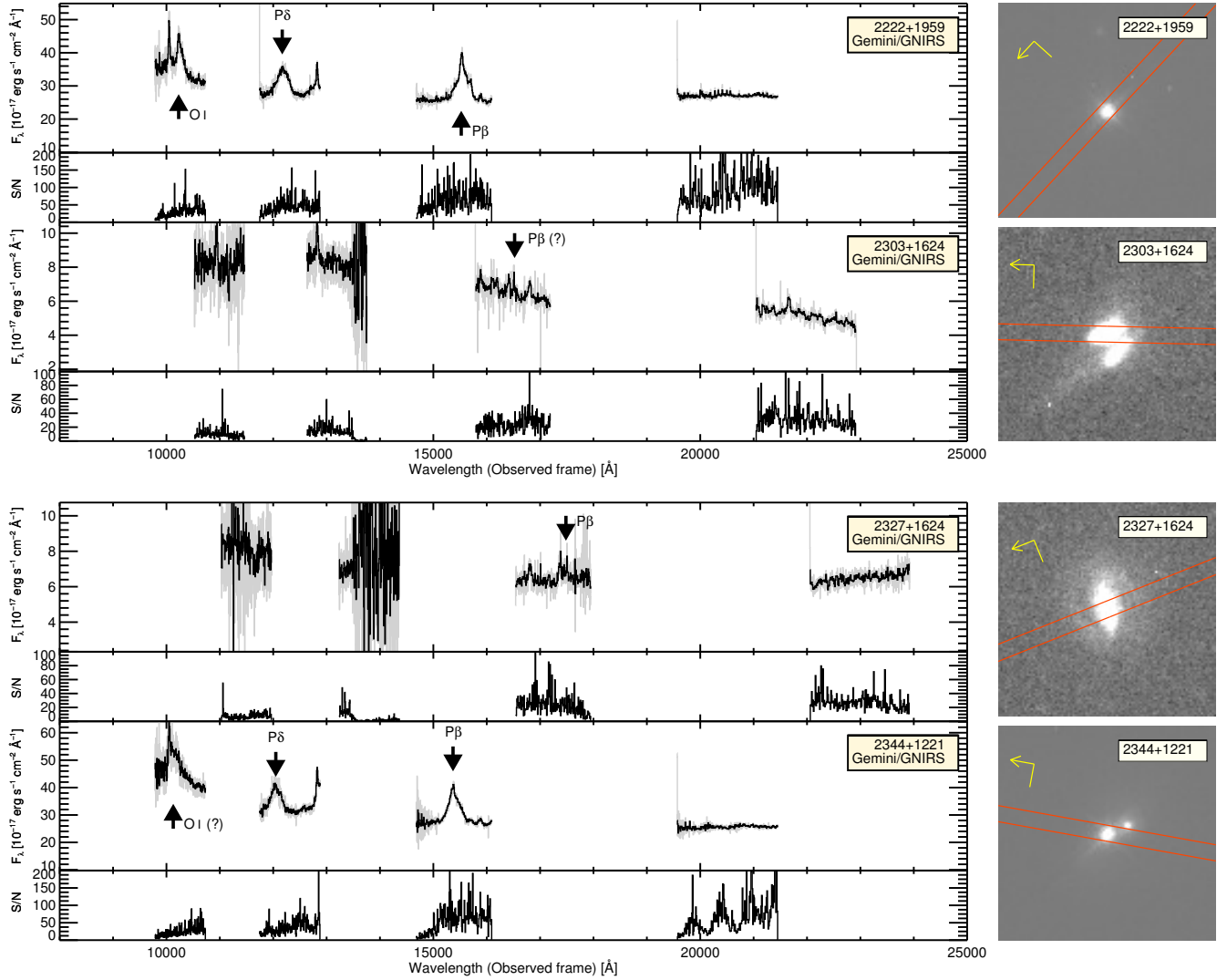


FIG. 2.— Continued

tively.

Note that the Gemini reduction packages do not include a flux calibration process for the GNIRS data, and it recommends achieving the flux calibration by scaling the observed spectrum to existing photometry or spectrum. For this reason, we perform the flux calibration by scaling the GNIRS spectrum to its J -, H -, and K -band magnitudes of 2MASS photometry. For 2303+1624, however, the J -band flux was abnormally small in comparison to the H - and K -band fluxes and had a large error, so we used y -band flux from the Pan-STARRS survey (Chambers et al. 2016) instead of the J -band flux. Due to our observational setup, the GNIRS spectra were taken at four disjointed orders, and each order was flux-scaled using an adjacent band. The two short orders ($\sim 10,000$ – $14,000$ Å) were scaled by J -band magnitude, and we used H - and K -band magnitudes for the third-order ($\sim 15,000$ – $18,000$ Å) and fourth-order ($\sim 20,000$ – $24,000$ Å), respectively. In order to check the reliability of the above GNIRS flux calibration, we obtained the SpeX spectrum for 1543+1937 (a bright and

point-like AGN in our data, see the *HST* image in Figure 2). Note that both SpeX and GNIRS data were obtained under clear weather and a decent seeing condition ($\sim 0''.7$). The SpeX data were flux-scaled using a single relative scaling factor using its K -band magnitude (see the paragraph below). Our comparison shows that the SpeX and GNIRS data match with each other within an $\sim 3\%$ difference from the second through the fourth orders. However, the shortest order of the GNIRS spectrum was $\sim 20\%$ different from the SpeX data. Although the shortest order of GNIRS spectra were not used in this study, we caution that the flux calibration of the shortest order could be off by about 20% .

In the next step, the NIR spectra from SpeX, FIRE, and IRCS were scaled to their K -band magnitudes of 2MASS photometry. This step was necessary, since there is a possibility of photon loss due to the different observing conditions and slit widths. We find that the scaling factors for the SpeX, FIRE, and IRCS spectra are not significant, with factors of 0.91 to 1.74 (a median of 1.18), and in particular, the scaling factors of the spectra obtained with SpeX are somewhat smaller with ~ 1.07 (from

TABLE 2
NIR SPECTRUM OF 0106+2603

λ (Å)	f_λ (erg s ⁻¹ cm ⁻² Å)	f_λ Uncertainty (erg s ⁻¹ cm ⁻² Å)
14439	4.6018E-17	2.2044E-17
14471	2.8404E-17	4.8711E-18
14504	1.9541E-17	4.8643E-18
14537	3.7478E-17	6.2486E-18
14570	2.5344E-17	3.7455E-18
14603	2.6977E-17	1.8525E-18
14636	3.1782E-17	2.4565E-18

NOTE. — This table represents only a part of the NIR spectrum of 0106+2603. All the NIR spectra of the 16 NIR-red AGNs obtained with the four telescopes are available in machine-readable format.

0.91 to 1.32). We also note that the AGN variability in NIR is a worrisome factor in this kind of calibration, since we are calibrating the spectra using the data that were taken at a different epoch. However, the NIR AGN variability is known to be generally small (~ 0.2 mag; e.g., Enya et al. 2002), so this flux calibration should be good to $\sim 20\%$ accuracy.

In total, we obtained 0.7–2.55 μm NIR spectra of 16 NIR-red AGNs at $z \sim 0.3$ with a moderate resolution of $R > 2000$ from the four instruments and telescopes. We summarize the observation information in Table 1.

2.3. Optical Observation

In addition to the NIR spectra, we obtained optical spectra for 12 NIR-red AGNs. Two (G. Canalizo & M. Lazarova) of us observed 10 NIR-red AGNs using the Echelle Spectrograph and Imager (ESI; Sheinis et al. 2002) on the Keck II telescope with a spectral wavelength range of 3900 Å to 11000 Å and a slit width of 1"0 to achieve a spectral resolution of $R \sim 4000$. Descriptions of the observations for the 10 NIR-red AGNs are given in Table 1. Information about the data reduction is given in Canalizo et al. (2012). Among the 10 spectra from the Keck/ESI observation, 5 were used in Canalizo et al. (2012).

For the remaining two NIR-red AGNs, we obtained the optical spectra from Data Release 12 (DR12) of the Sloan Digital Sky Survey (SDSS). The fiber diameter is 3"0, and the spectral coverage of the SDSS spectra is 3800 Å to 9200 Å with a spectral resolution of 1500–2500.

For these optical spectra, their slit widths and fiber sizes are somewhat larger than the slit widths for the NIR spectra. Although the inconsistency of the slit width can introduce discrepancies in the spectral properties between the optical and NIR spectra, the effects on the spectral properties measured in this study are negligible due to the following reasons: (i) broad emission lines (BELs) come from the nuclear region, and (ii) we use only the optical or NIR spectrum to fit the continuum.

3. HIGH-S/N AND MEDIUM-RESOLUTION SPECTRA

We show the fully reduced NIR spectra and the *HST* images of the 16 NIR-red AGNs in Figure 2, and the spectra are available in machine-readable form in Table 2. Moreover, Figure 2 also shows the S/N of each

TABLE 3
OPTICAL SPECTRUM OF 0106+2603

λ (Å)	f_λ (erg s ⁻¹ cm ⁻² Å)	f_λ Uncertainty (erg s ⁻¹ cm ⁻² Å)
3899.4	8.3145E-17	6.4623E-18
3900.4	5.3173E-17	1.1044E-17
3901.3	2.6999E-17	3.4251E-18
3902.3	6.7212E-17	1.8250E-17
3903.3	1.2357E-16	1.4382E-17
3904.3	1.4238E-16	3.2512E-18
3905.2	1.1617E-16	1.4047E-17

NOTE. — This table represents only a part of the optical spectrum of 0106+2603. The optical spectra of the 12 NIR-red AGNs from the Keck/ESI observation and SDSS data are available in machine-readable format.

spectrum, and we mark several interesting lines such as $\text{P}\alpha$ (1.875 μm), $\text{P}\beta$ (1.282 μm), $\text{P}\gamma$ (1.094 μm), $\text{P}\delta$ (1.005 μm), $\text{P}\epsilon$ (0.955 μm), $\text{P}\zeta$ (0.923 μm), $[\text{Fe II}]$ (1.600 and 1.257 μm), O I (1.129 and 0.845 μm), and He I (1.083 μm).

In addition to the NIR spectra, Figure 3 shows the reduced optical spectra of the 12 NIR-red AGNs, and several lines of $[\text{O II}]$ (3727 Å), $\text{H}\gamma$ (4340 Å), $\text{H}\beta$ (4861 Å), $[\text{O III}]$ (4959 and 5007 Å), $\text{H}\alpha$ (6563 Å), and $[\text{N II}]$ (6548 and 6583 Å) are marked on the spectra. The optical spectra are given in ascii format in Table 3.

3.1. Spectral Fitting of Hydrogen Lines

In this subsection, we describe how the BELs of $\text{H}\beta$, $\text{H}\alpha$, $\text{P}\beta$, and $\text{P}\alpha$ are fitted to measure the luminosities and FWHMs. The fitting of these lines starts with the identification of the line, and we find the $\text{H}\beta$, $\text{H}\alpha$, $\text{P}\beta$, and $\text{P}\alpha$ lines in 11, 12, 14, and 6 NIR-red AGNs, respectively.

After the line identification, we correct the spectra for the Galactic extinction (Schlafly & Finkbeiner 2011) using the reddening law of Fitzpatrick (1999). Then, we transform the spectra to the rest-frame and fit the continua for the $\text{H}\beta$, $\text{H}\alpha$, $\text{P}\beta$, and $\text{P}\alpha$ lines. For $\text{H}\alpha$, $\text{P}\beta$, and $\text{P}\alpha$, the continuum around each line is fitted with a single power law, however, an additional Fe component is required for the $\text{H}\beta$ line. The Fe blends are determined by scaling and broadening the Fe template from the spectrum of IZw1 (Boroson & Green 1992), and this procedure is performed with MPFIT (Markwardt 2009) using Interactive Data Language (IDL). As an example, Figure 4 shows the spectra around the $\text{H}\beta$, $\text{H}\alpha$, $\text{P}\beta$, and $\text{P}\alpha$ lines, along with the fitted continuum models, and the continuum-subtracted spectra. Note that we omit the stellar component for the continuum fit, since the stellar component can be fit by the power law in such narrow wavelength ranges.

We note that several lines exist around the $\text{H}\beta$, $\text{H}\alpha$, $\text{P}\beta$, and $\text{P}\alpha$ lines (e.g., $\text{H}\gamma$ λ 4340, $[\text{O III}]$ λ 4956, 5007 doublet, $[\text{S II}]$ λ 6716, 6731 doublet, and O I λ 11287). Hence, the continuum-fitting regions are chosen to avoid the nearby lines.

After the continuum subtraction, we model the narrow lines using the $[\text{O III}]$ λ 4956, 5007 and $[\text{S II}]$ λ 6716, 6731 doublets as templates. In order to fit the $[\text{S II}]$ lines, we use two single Gaussian functions. However, the $[\text{O III}]$ lines require double Gaussian functions for their

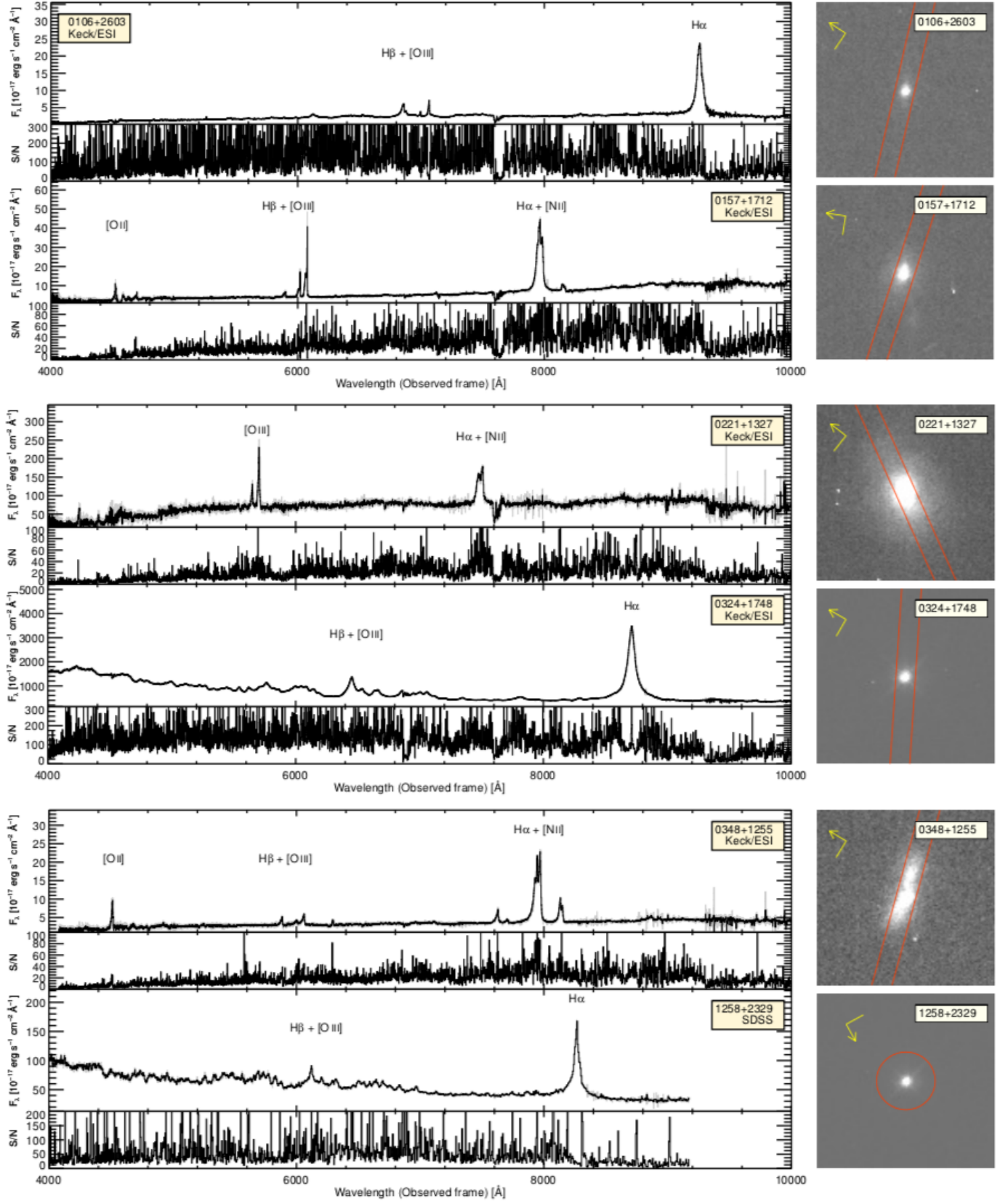


FIG. 3.— (Left) Optical spectra of 12 NIR-red AGNs and their S/N. The gray and black lines indicate observed and binned spectra in the observed frame, and we binned the spectra with the spectral resolution. We mark several emission lines in the optical wavelength region, such as [O II] (3727 Å), H γ (4340 Å), H β (4861 Å), [O III] (4959 and 5007 Å), H α (6563 Å), and [N II] (6548 and 6583 Å). (Right) *HST* images of 12 NIR-red AGNs. The red boxes and yellow arrows are identical to those in Figure 2, and the red open circles indicate SDSS fiber diameters.

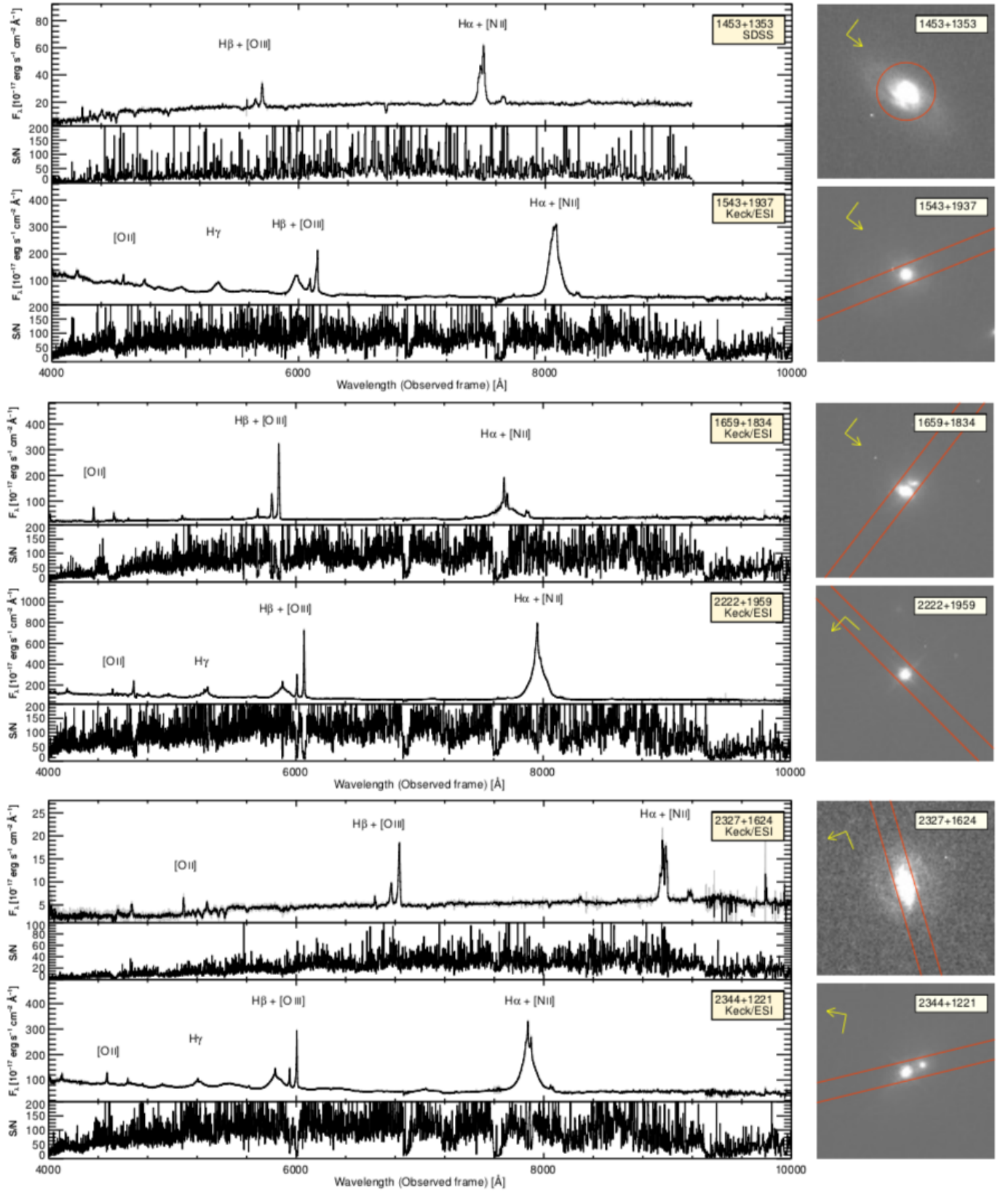


FIG. 3.— Continued

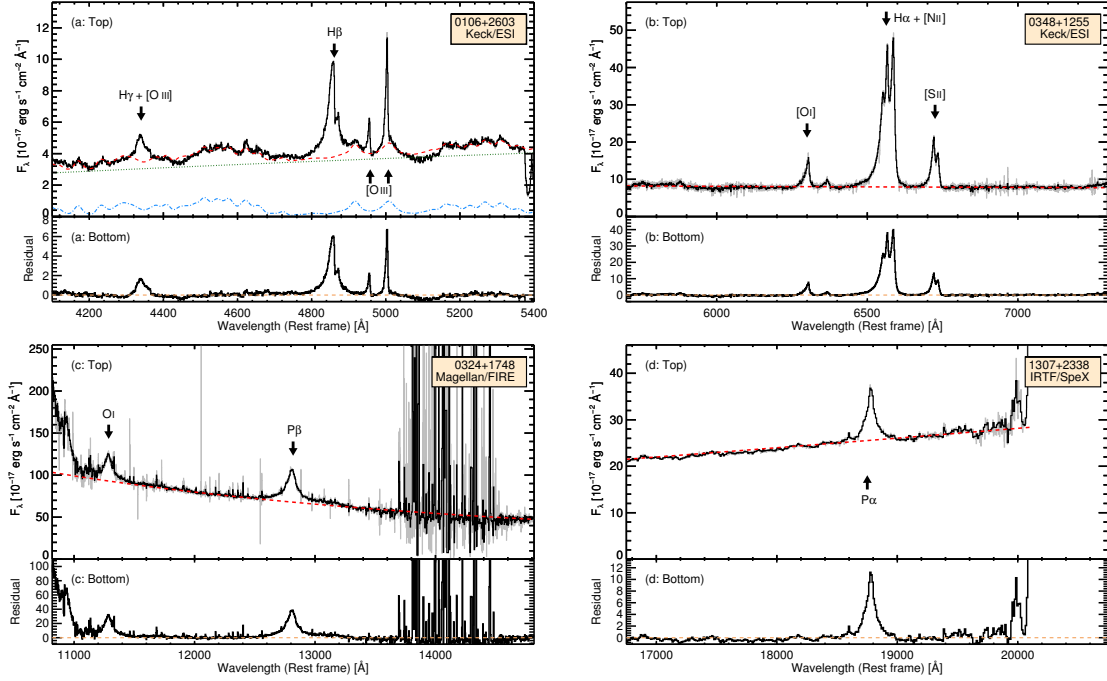


FIG. 4.— (a) Top: the optical spectrum of 0106+2603 obtained with the ESI on Keck telescope. The black solid line denotes the optical spectrum around the $H\beta$ line, and this spectrum includes several interesting emission lines, such as $H\gamma$ (4341 Å), [O III] (4363, 4959, and 5007 Å), and $H\beta$ (4861 Å). The fitted model continuum spectrum is represented by the red dashed line, and this model is composed of a power-law component (the green dotted line) and a component for the Fe blends (the sky blue dot-dashed line). Bottom: the fitted model continuum-subtracted spectrum is represented, and this continuum-subtracted spectrum is used for estimating the line luminosity and FWHM. (b) The original and residual spectrum around the $H\alpha$ line of 0348+1255, which is obtained with Keck/ESI. The meanings of the black solid line and the red dashed line are identical to those in panel (a). The black arrows represent [O I] (6300 Å), $H\alpha$ (6563 Å), [N II] (6548 and 6583 Å), and [S II] (6716 and 6731 Å). (c) The original and residual spectrum around the $P\beta$ line of 0324+1748, which is taken with Magellan/FIRE. The meanings of the black solid line and the red dashed line are identical to those in panel (a), and $P\beta$ and O I (1.1287 μm) are marked with the black arrows. (d) The original and residual spectrum around the $P\alpha$ line of 1307+2338, which is obtained with IRTF/SpEx. The meanings of the black solid line and the red dashed line are identical to those in panel (a), and the $P\alpha$ line is marked with the black arrow.

asymmetric blue wings (Greene & Ho 2005). Although Greene & Ho (2005) suggest that the [O III] lines are not appropriate as a template for the narrow lines of unobscured type 1 quasars due to the blue wings, this template gives better results than the [S II] template when fitting the narrow components of the $H\beta$ line, for a part of our NIR-red AGN sample. However, since the [S II] template fits the narrow components of $H\alpha$, $P\beta$, and $P\alpha$ lines better, the template from the [S II] lines is primarily used to fit these lines, except when the [S II] lines are not detected.

Moreover, the [S II] narrow line template is also used for fitting the [N II] $\lambda\lambda 6548, 6583$ doublet and the narrow component of the hydrogen lines. For the fitting of the [N II] lines, we fit the $H\alpha$ and [N II] lines simultaneously. The width of the [N II] line is fixed to the width of the narrow line template, and its flux ratio is fixed to 2.96 (Kim et al. 2006).

We note that the narrow line template from the [O III] lines is used for 0106+2603 ($H\beta$ and $H\alpha$), 0157+1712 ($H\beta$), 0221+1327 ($H\beta$, $H\alpha$, $P\beta$, and $P\alpha$), 0348+1255 ($H\beta$), 1659+1834 ($H\beta$), 2222+1959 ($H\beta$, $H\alpha$, and $P\beta$), 2327+1624 ($H\beta$), and 2344+1221 ($H\beta$), and the narrow line template from the [S II] lines is used for 0157+1712 ($H\alpha$ and $P\beta$), 0348+1255 ($H\alpha$ and $P\beta$), 1453+1353 ($H\alpha$ and $P\alpha$), 1543+1937 ($H\alpha$), 1659+1834 ($H\alpha$, $P\beta$, and $P\alpha$), 2327+1624 ($H\alpha$), and 2344+1221 ($H\alpha$ and $P\beta$). The measured FWHMs and luminosities of the [O III],

[N II], and [S II] lines are listed in Table 4.

For 1258+2329 ($P\alpha$) and 2303+1624 ($P\beta$), the narrow lines cannot be modeled due to the absence of the [O III] and [S II] lines, so Gaussian functions were fit to the lines. One of the fitted components is classified as the narrow component due to its FWHM being less than 600 km s^{-1} .

Using the model of the narrow component, we simultaneously fit the broad-line ($\text{FWHM} > 600 \text{ km s}^{-1}$) with a single or double Gaussian function. Figure 5 shows the $H\beta$, $H\alpha$, $P\beta$, and $P\alpha$ lines of NIR-red AGNs and its fitted models. For the fit, a single, double, or multiple Gaussian functions are used depending on the S/N and the resolution of the spectra. For example, many of the broad lines in NIR spectra are fitted with a single or double Gaussian function due to the limited spectral resolution. Kim et al. (2010) showed using 26 unobscured type 1 AGNs with high-S/N and high-resolution spectra that the application of the single/double component Gaussian fits to data with a limited spectral resolution and S/N can produce slightly biased line flux/FWHM values with respect to the multi-component (> 2 components) fits, which is the method to use if high-S/N, high-resolution data were available. Based on the results, they derived the correction factors to correct for the systematic bias, which are $\text{flux}_{\text{multi}}/\text{flux}_{\text{double}} = 1.05$, $\text{flux}_{\text{multi}}/\text{flux}_{\text{single}} = 1.06$, $\text{FWHM}_{\text{multi}}/\text{FWHM}_{\text{double}} = 0.85$, and $\text{FWHM}_{\text{multi}}/\text{FWHM}_{\text{single}} = 0.91$ (Kim et al. 2010; Kim & Im 2018). We adopt these values to con-

TABLE 4
LINE MEASUREMENTS OF [O III], [N II], AND [S II] LINES

Object Name	[O III] $\lambda 5007$		[N II] $\lambda 6548$		[S II] $\lambda 6716$	
	L (10^{38} erg s $^{-1}$)	FWHM (km s $^{-1}$)	L (10^{38} erg s $^{-1}$)	FWHM (km s $^{-1}$)	L (10^{38} erg s $^{-1}$)	FWHM (km s $^{-1}$)
0106+2603	29.72 \pm 1.45	359.9 \pm 36.2	11.75 \pm 0.11	359.9 \pm 36.2	—	—
0157+1712	41.72 \pm 4.01	988.4 \pm 63.8	11.58 \pm 0.14	563.7 \pm 20.7	7.510 \pm 0.395	563.7 \pm 20.7
0221+1327	154.6 \pm 12.3	539.5 \pm 54.9	22.73 \pm 0.46	539.5 \pm 54.9	—	—
0234+2438	—	—	—	—	—	—
0324+1748	—	—	—	—	—	—
0348+1255	21.54 \pm 0.74	718.7 \pm 25.7	20.81 \pm 0.20	595.8 \pm 6.8	20.62 \pm 0.35	595.8 \pm 6.8
1258+2329	—	—	—	—	—	—
1307+2338	—	—	—	—	—	—
1453+1353	—	—	10.25 \pm 0.38	695.5 \pm 47.5	4.699 \pm 0.349	695.5 \pm 47.5
1543+1937	483.2 \pm 23.5	808.2 \pm 79.0	55.58 \pm 0.80	387.2 \pm 10.8	19.70 \pm 1.03	387.2 \pm 10.8
1659+1834	344.2 \pm 5.4	628.7 \pm 22.1	30.97 \pm 0.35	501.2 \pm 5.1	27.22 \pm 0.40	501.2 \pm 5.1
2222+1952	—	—	—	—	—	—
2222+1959	987.2 \pm 41.4	538.9 \pm 41.8	84.91 \pm 0.84	538.9 \pm 41.8	—	—
2303+1624	—	—	—	—	—	—
2327+1624	116.3 \pm 20.8	719.6 \pm 77.7	29.92 \pm 0.52	518.9 \pm 33.1	13.76 \pm 1.59	518.9 \pm 33.1
2344+1221	248.9 \pm 10.1	449.3 \pm 30.9	52.69 \pm 0.99	301.1 \pm 10.0	17.00 \pm 0.97	301.1 \pm 10.0

NOTE. — The listed fluxes are not corrected from the dust extinction caused by their host galaxies.

vert the single/double Gaussian fit results to the multi-component fitting results. Moreover, the FWHMs are corrected for the instrumental resolution as $\text{FWHM}^2 = \text{FWHM}_{\text{obs}}^2 - \text{FWHM}_{\text{inst}}^2$.

We note that the FWHM of the $P\beta$ line of 2327+1624 is not measured, because the $P\beta$ line is fitted by two Gaussian components that are broadly split. The broadly split components yield four half-maximum points, so the FWHM cannot be measured.

Strong correlations between the FWHMs of the Balmer and Paschen lines have been established for unobscured type 1 quasars (Landt et al. 2008; Kim et al. 2010). A tight correlation between the two quantities for our sample would imply that the luminosities originate from the same BLR, and the contribution of the narrow component is negligible. As shown in Figure 6, the measured FWHMs of Paschen lines are similar to those of Balmer lines, and the correlations between the two quantities are similar to those of unobscured type 1 quasars.

In total, we obtain the broad line-luminosities and FWHMs of 7 $H\beta$, 12 $H\alpha$, 12 $P\beta$, and 6 $P\alpha$ lines. The measured luminosities and FWHMs of the hydrogen lines for broad and narrow components are summarized in Table 5 and Table 6, respectively.

4. REDDENING

In this section, we assume that the red colors of NIR-red AGNs originate from the dust extinction in their host galaxies, as shown in several previous studies (Glikman et al. 2007; Urrutia et al. 2008, 2009; Kim & Im 2018). Hence, measuring the color excess, $E(B - V)$, is important for investigating the intrinsic, i.e., un-reddened properties of dusty AGNs. In the following subsections, $E(B - V)$ values are derived using two methods, comparison of line-luminosity ratios and continuum slopes between unobscured and NIR-red AGNs. In this section, we use the reddening law, $k(\lambda)$, of Fitzpatrick (1999), based on the Galactic extinction curve from 1000 Å to 3.5 μm with $R_V = 3.1$.

4.1. Reddening derived from line-luminosity ratios

We measure the reddening from line-luminosity ratios ($E(B - V)_{\text{line}}$) of NIR-red AGNs by using four broad line-luminosity ratios of Balmer to Paschen lines ($L_{H\beta}/L_{P\beta}$, $L_{H\alpha}/L_{P\beta}$, $L_{H\beta}/L_{P\alpha}$, and $L_{H\alpha}/L_{P\alpha}$). We use the correlation between the Balmer and Paschen line luminosities of 37 low-redshift ($z < 0.5$) and bright ($J < 14$ or $K < 14.5$ mag) unobscured type 1 quasars adopted from Kim et al. (2010) as their intrinsic line-luminosity ratios. By comparing the line-luminosity ratios, the $E(B - V)_{\text{line}}$ values can be measured for 10 out of the 16 NIR-red AGNs.

The $E(B - V)_{\text{line}}$ values are computed by varying the amount of dust-reddening to minimize χ^2 , which is a function of the line-luminosity ratios of NIR-red AGNs ($R_{\text{obs},i,j} = L_{\text{obs},\lambda j}/L_{\text{obs},\lambda i}$) and unobscured type 1 quasars ($R_{\text{int},i,j} = L_{\text{int},\lambda j}/L_{\text{int},\lambda i}$), expressed as

$$\chi^2 = \sum_{i,j=1}^N \frac{(R_{\text{obs},i,j} - E(R_{\text{int},i,j}))^2}{\sigma_{i,j}^2}. \quad (1)$$

Here, N is the number of line-luminosity ratios, $\sigma_{i,j}$ are the combined uncertainties of the line-luminosity ratios and the adopted correlations from Kim et al. (2010), and E is a function for the dust-reddening expressed as

$$\log \left(\frac{E(R_{\text{int},i,j})}{R_{\text{int},i,j}} \right) = \frac{E(B - V)}{1.086} (k(\lambda i) - k(\lambda j)). \quad (2)$$

For estimating the uncertainty of $E(B - V)_{\text{line}}$, we perform 1000 Monte-Carlo simulations. We calculate new line-luminosity ratios by adding the measurement uncertainties of the line luminosities randomly to the observed line luminosities. The standard deviation of the 1000 newly measured $E(B - V)_{\text{line}}$ values is taken as the uncertainty of the $E(B - V)_{\text{line}}$.

In Figure 7, we compare the observed and the dust-extinction-corrected line luminosities with the $E(B - V)_{\text{line}}$ values. The measured $E(B - V)_{\text{line}}$ values and uncertainties for the 10 NIR-red AGNs are summarized in Table 7.

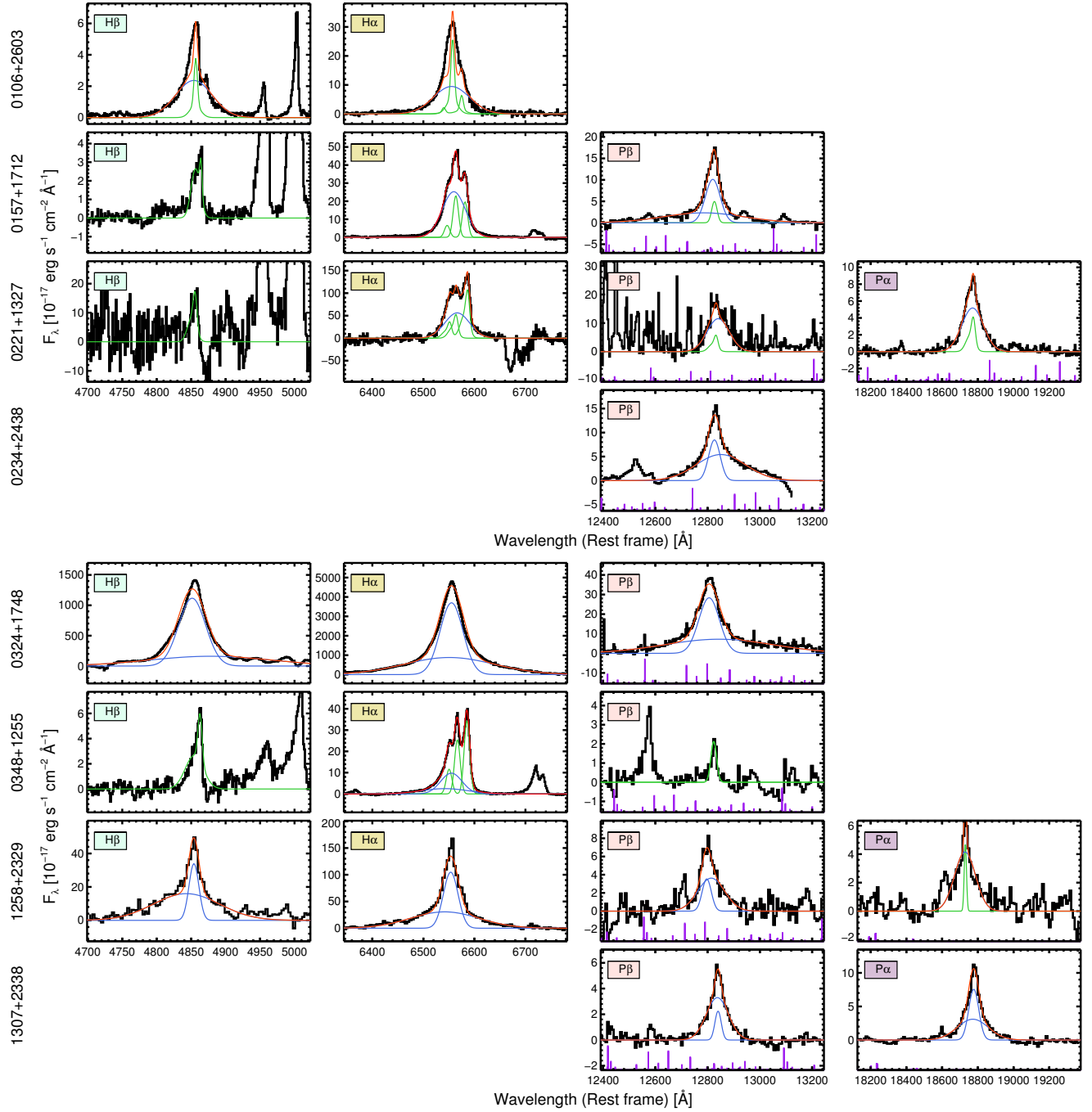


FIG. 5.— Results of the fitting of the $H\beta$, $H\alpha$, $P\beta$, and $P\alpha$ lines. The black lines indicate the continuum-subtracted observed spectra in the rest-frame. The red lines represent the best-fit model, and the green and blue lines represent the narrow and broad components, respectively. Moreover, for the $P\beta$ and $P\alpha$ figures, the purple lines at the bottom show the sky OH emission lines.

4.2. Reddening derived from continuum slopes

We measure the color excess values from continuum slope ($E(B-V)_{\text{cont}}$) of the NIR-red AGNs by comparing the observed spectrum, $f(\lambda)$, to a model spectrum. The model spectrum combines a reddened quasar composite, $Q(\lambda)$, and a reddened stellar template, $S(\lambda)$. The intrinsic quasar composite, $Q_0(\lambda)$, is adopted from Glikman et al. (2006), which is a composition of an optical quasar composite (Brotherton et al. 2001) and an NIR quasar composite (Glikman et al. 2006). They used unobscured type 1 quasars for constructing the optical and

NIR quasar composites. For the intrinsic stellar template, $S_0(\lambda)$, we use K (MJD=51816, plate=396, and fiber=605), F (MJD=51990, plate=289, and fiber=5), and G (MJD=51957, plate=273, and fiber=304) type stellar spectra adopted from SDSS, since the K, F, and G type stars are the most dominant populations of the stellar composite template for NIR-red AGNs (Canalizo et al. 2012).

In order to fit the $E(B-V)_{\text{cont}}$ values, we fit the model spectrum to the observed spectrum, and the fitting func-

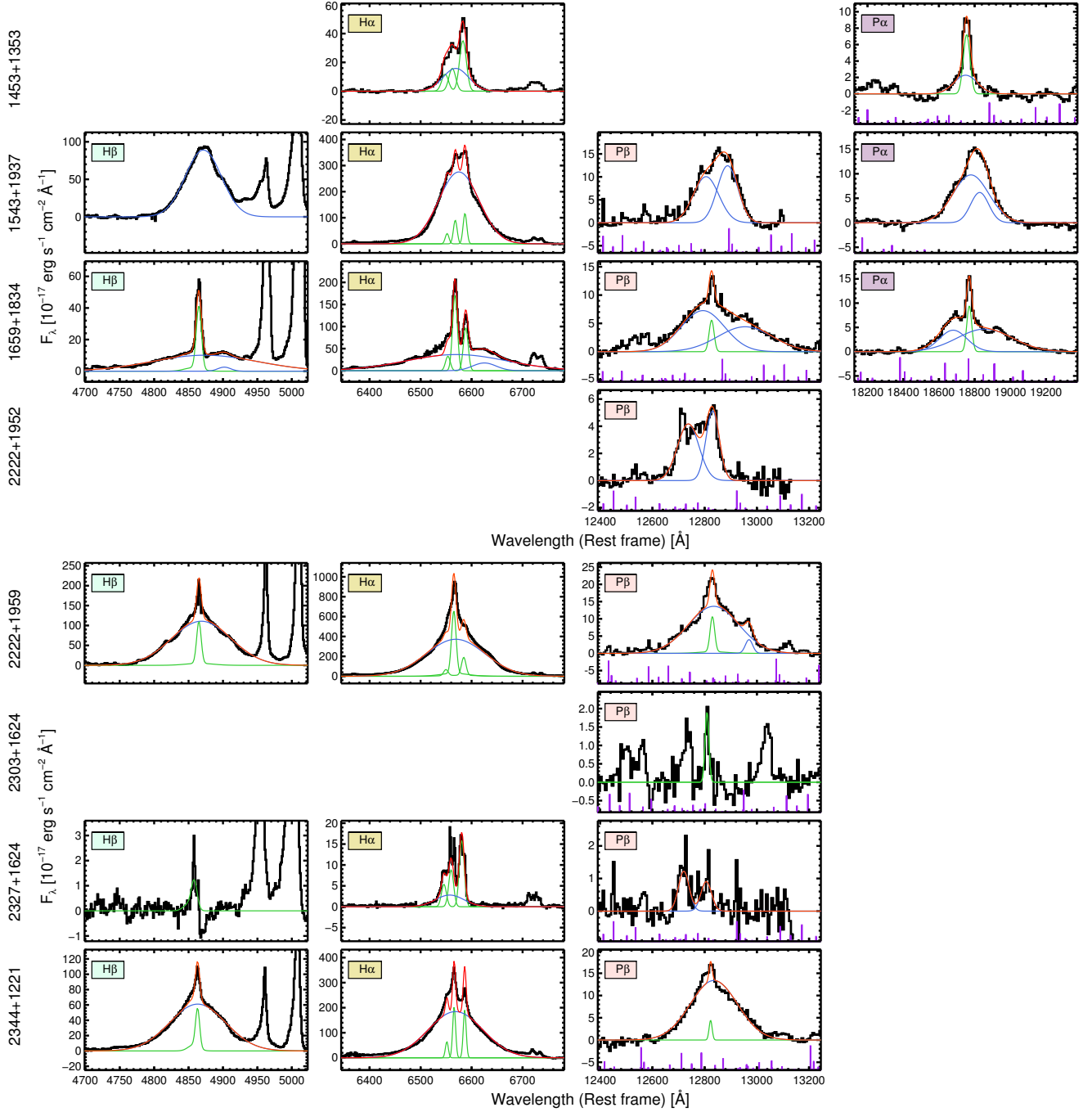


FIG. 5.— Continued

tion has a form of

$$f(\lambda) = Q(\lambda) + S(\lambda). \quad (3)$$

Here, $Q(\lambda)$ and $S(\lambda)$ are the reddened spectra of $Q_0(\lambda)$ and $S_0(\lambda)$, respectively, with their $E(B - V)$ values as

$$\log \left(\frac{X(\lambda)}{X_0(\lambda)} \right) = - \frac{k(\lambda)E(B - V)_X}{1.086}, \quad (4)$$

where $E(B - V)_Q$ is taken as $E(B - V)_{\text{cont}}$. Here, $X(\lambda)$ denotes $Q(\lambda)$ or $S(\lambda)$, and $X_0(\lambda)$ is $Q_0(\lambda)$ or $S_0(\lambda)$.

For the fit, we use only a limited wavelength range

(3790–10000 Å), because Glikman et al. (2007) reported that fitting with the optical and NIR combined spectrum yields extremely poor results for one-third of red AGNs. Moreover, to exclude strong emission lines, wavelength regions of 3790–4700, 5100–6400, and 6700–10000 Å are used. There are remaining moderate emission lines (e.g., He I λ 3889, He ϵ λ 3970, H δ λ 4102, H γ λ 4340, He I λ 5876, [O I] λ λ 6300, 6364, and O I λ 8447), but the effects on the fit are negligible. In order to find the most likely stellar template, we calculate χ^2 values for the fits with the K, F, and G type star spectra, and the fit with the minimum χ^2 is used as the best fit. From this fitting

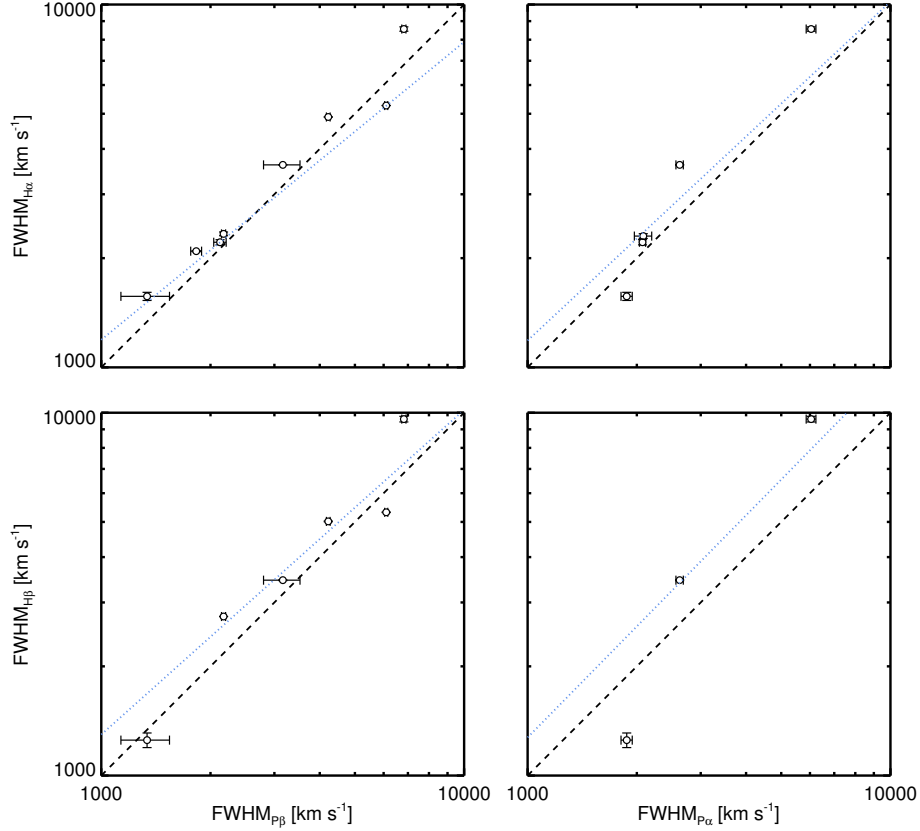


FIG. 6.— Comparisons of the FWHMs of the Balmer and Paschen lines. The black dashed lines show the two quantities are identical, and the blue dotted lines denote the adopted correlation of unobscured type 1 quasars from Kim et al. (2010).

procedure, we measure the $E(B - V)_{\text{cont}}$ values for 12 NIR-red AGNs, and Figure 8 shows the fitting results. The measured $E(B - V)_{\text{cont}}$ values and uncertainties are summarized in Table 7.

4.3. Discussion for the two types of reddening

We compare the $E(B - V)_{\text{line}}$ values to the $E(B - V)_{\text{cont}}$ values for the 10 NIR-red AGNs that have both $E(B - V)_{\text{line}}$ and $E(B - V)_{\text{cont}}$ in Figure 9. The two types of $E(B - V)$ values are consistent, but there is a weak trend of $E(B - V)_{\text{cont}} - E(B - V)_{\text{line}} \sim 0.281$. We estimate the Pearson correlation coefficient between the two quantities. For estimating the coefficient, we exclude 0324+1748, which has negative values for both types of $E(B - V)$, and assume that the negative $E(B - V)$ values ($E(B - V)_{\text{line}}$ values of 1258+2329 and 2222+1959) are 0. The measured coefficient is 0.911, and the rms scatter with respect to a one-to-one correlation is 0.223. This result supports that the two measurements of $E(B - V)$ are mutually verified.

Moreover, we compare the two types of $E(B - V)$ values to the $E(B - V)$ values adopted from Canalizo et al. (2012; hereafter, $E(B - V)_{\text{C12}}$), and this comparison is shown in Figure 9. They measured the $E(B - V)_{\text{C12}}$ by comparing the observed continuum spectrum to the SDSS composite QSO spectrum (Vanden Berk et al. 2001) reddened with a Small Magellanic Cloud reddening law (Bouchet et al. 1985), and five NIR-red

AGNs (0157+1712, 0221+1327, 0348+1255, 1659+1834, and 2327+1624) are overlapped with our sample. They showed that the $E(B - V)_{\text{C12}}$ values were generally consistent with the $E(B - V)$ values derived by using Balmer decrements, and the difference between this two quantities was ~ 0.3 . Our $E(B - V)_{\text{cont}}$ and $E(B - V)_{\text{line}}$ values are generally but somewhat weakly consistent with the $E(B - V)_{\text{C12}}$ values. Between the $E(B - V)_{\text{cont}}$ and $E(B - V)_{\text{C12}}$ values, the Pearson correlation coefficient is 0.579, and the rms scatter is 0.484. For the $E(B - V)_{\text{line}}$ values, the result is generally same as the coefficient is 0.663 with the rms scatter of 0.582. We found a trend that the $E(B - V)$ values from this work is less than the $E(B - V)_{\text{C12}}$ values, as much as $\Delta E(B - V) \sim 0.520$, but this trend is not significant due to small number statistics.

Unlike our results, previous studies (Glikman et al. 2007; Kim & Im 2018) reported that the two types of $E(B - V)$ values are far from a one-to-one correlation. The Pearson correlation coefficient between the two quantities is only -0.21, with an rms scatter of 0.68 (Kim & Im 2018).

In the previous studies, the $E(B - V)_{\text{cont}}$ values are from Glikman et al. (2007) and Urrutia et al. (2009), and the $E(B - V)_{\text{line}}$ values are from Glikman et al. (2007). To obtain the $E(B - V)_{\text{cont}}$ values, they fit the continua using the quasar component only, without the stellar component. In this study, considering the contin-

TABLE 5
HYDROGEN LINE MEASUREMENTS FOR THE BROAD COMPONENT

Object Name	H β		H α		P β		P α	
	FWHM (km s ⁻¹)	L (10 ⁴⁰ erg s ⁻¹)	FWHM (km s ⁻¹)	L (10 ⁴⁰ erg s ⁻¹)	FWHM (km s ⁻¹)	L (10 ⁴⁰ erg s ⁻¹)	FWHM (km s ⁻¹)	L (10 ⁴⁰ erg s ⁻¹)
0106+2603	3281±5	1.000±0.003	3227±8	5.312±0.028	—	—	—	—
0157+1712	—	—	2090±7	2.009±0.017	1827±63	2.133±0.102	—	—
0221+1327	—	—	2212±36	1.875±0.070	2125±84	0.682±0.043	2073±40	0.436±0.013
0234+2438	—	—	—	—	1515±77	5.735±0.202	—	—
0324+1748	2744±0	339.5±1.6	2333±28	1513±3	2173±28	24.67±0.42	—	—
0348+1255	—	—	2539±325	1.027±0.038	—	—	—	—
1258+2329	1252±58	5.601±0.137	1569±41	19.75±0.39	1337±204	1.368±0.152	1876±67	1.342±0.084
1307+2338	—	—	—	—	1125±106	1.040±0.073	1113±35	2.997±0.129
1453+1353	—	—	2301±35	0.541±0.033	—	—	2083±114	0.201±0.017
1543+1937	3456±10	9.554±0.038	3615±4	44.27±0.10	3165±365	3.976±0.379	2624±62	5.254±0.193
1659+1834	9603±171	1.603±0.023	8561±120	8.117±0.051	6822±90	2.128±0.036	6045±187	2.135±0.058
2222+1952	—	—	—	—	3212±502	3.647±0.201	—	—
2222+1959	5316±9	16.28±0.04	5268±4	73.07±0.12	6099±60	3.705±0.069	—	—
2303+1624	—	—	—	—	—	—	—	—
2327+1624	—	—	2554±71	0.940±0.050	—	0.450±0.093	—	—
2344+1221	5018±13	7.423±0.030	4899±5	29.56±0.07	4223±50	3.273±0.054	—	—

NOTE. — The listed fluxes of H β , H α , P β , and P α lines are not corrected from the dust extinction caused by their host galaxies.

TABLE 6
HYDROGEN LINE MEASUREMENTS FOR THE NARROW COMPONENT

Object Name	H β		H α		P β		P α	
	L (10 ³⁸ erg s ⁻¹)	FWHM (km s ⁻¹)	L (10 ³⁸ erg s ⁻¹)	FWHM (km s ⁻¹)	L (10 ³⁸ erg s ⁻¹)	FWHM (km s ⁻¹)	L (10 ³⁸ erg s ⁻¹)	FWHM (km s ⁻¹)
0106+2603	20.17±0.03	359.9±36.2	140.6±0.8	359.9±36.2	—	—	—	—
0157+1712	6.869±0.300	988.4±63.8	40.24±0.71	563.7±20.7	17.18±2.95	563.7±20.7	—	—
0221+1327	10.73±4.40	539.5±54.9	32.92±1.62	539.5±54.9	3.615±0.656	539.5±54.9	2.566±0.124	539.5±54.9
0234+2438	—	—	—	—	—	—	—	—
0324+1748	—	—	—	—	—	—	—	—
0348+1255	14.88±0.10	718.7±25.7	45.51±0.60	595.8±6.8	7.530±0.776	595.8±6.8	—	—
1258+2329	—	—	—	—	—	—	15.77±4.82	190.3±36.1
1307+2338	—	—	—	—	—	—	—	—
1453+1353	—	—	13.76±0.87	695.5±47.5	—	—	17.55±0.65	695.5±47.5
1543+1937	—	—	128.0±2.1	387.2±10.8	—	—	—	—
1659+1834	35.11±9.53	628.7±22.1	161.5±2.0	501.2±5.1	10.57±0.65	501.2±5.1	26.17±1.27	501.2±5.1
2222+1952	—	—	—	—	—	—	—	—
2222+1959	144.6±1.3	538.9±41.8	875.9±5.3	538.9±41.8	11.71±0.86	538.9±41.8	—	—
2303+1624	—	—	—	—	7.887±3.145	397.4±115.9	—	—
2327+1624	7.587±9.783	719.6±77.7	49.27±1.45	518.9±33.1	—	—	—	—
2344+1221	60.26±0.91	449.3±30.9	166.5±2.7	301.1±10.0	6.810±1.109	301.1±10.0	—	—

NOTE. — The listed fluxes are not corrected from the dust extinction caused by their host galaxies.

uum spectra of the most of NIR-red AGNs are dominated by the quasar component, the measurement technique for the $E(B-V)_{\text{cont}}$ is almost the same, and it is hard to believe that the contrasting result comes from the discrepancy of the $E(B-V)_{\text{cont}}$ values.

However, in order to measure the $E(B-V)_{\text{line}}$ values, Glikman et al. used somewhat different way. They measured the $E(B-V)_{\text{line}}$ values using Balmer decrements (hereafter, $E(B-V)_{\text{BD1}}$). The $E(B-V)_{\text{BD1}}$ values were obtained by following formula:

$$E(B-V)_{\text{BD1}} = \frac{1.086}{k(\text{H}\beta) - k(\text{H}\alpha)} \ln \left(\frac{[F_{\text{H}\alpha}/F_{\text{H}\beta}]_{\text{measured}}}{[F_{\text{H}\alpha}/F_{\text{H}\beta}]_{\text{FBQS}}} \right). \quad (5)$$

Here, $k(X)$ is the extinction law of Calzetti et al. (1994) at the wavelength of the X line, and $[F_{\text{H}\alpha}/F_{\text{H}\beta}]_{\text{measured}}$ and $[F_{\text{H}\alpha}/F_{\text{H}\beta}]_{\text{FBQS}}$ are the $F_{\text{H}\alpha}/F_{\text{H}\beta}$ from the spectra of red quasars and the Faint Images of the Radio Sky

at Twenty-Centimeters (FIRST) Bright Quasar Survey (FBQS; Gregg et al. 1996) composite spectrum, respectively. In this equation, the $[F_{\text{H}\alpha}/F_{\text{H}\beta}]_{\text{FBQS}}$ is used as the intrinsic $F_{\text{H}\alpha}/F_{\text{H}\beta}$ of red quasars, which is a fixed value of 4.526 when only the broad component is treated (Glikman et al. 2007).

Using this technique, we can measure the $E(B-V)_{\text{BD1}}$ values for seven NIR-red AGNs, and they are summarized in Table 7. We compare the $E(B-V)_{\text{BD1}}$ values to the $E(B-V)_{\text{line}}$ and $E(B-V)_{\text{cont}}$ values in Figure 10. For the $E(B-V)_{\text{BD1}}$ values versus $E(B-V)_{\text{line}}$ values, six NIR-red AGNs are used, and the measured Pearson correlation coefficient is 0.314 with an rms scatter of 0.257. For the comparison between the $E(B-V)_{\text{BD1}}$ and $E(B-V)_{\text{cont}}$ values, we used seven NIR-red AGNs that have both quantities, and the Pearson coefficient and the rms scatter are 0.709 and 0.255, respectively.

In order to figure out what makes this difference,

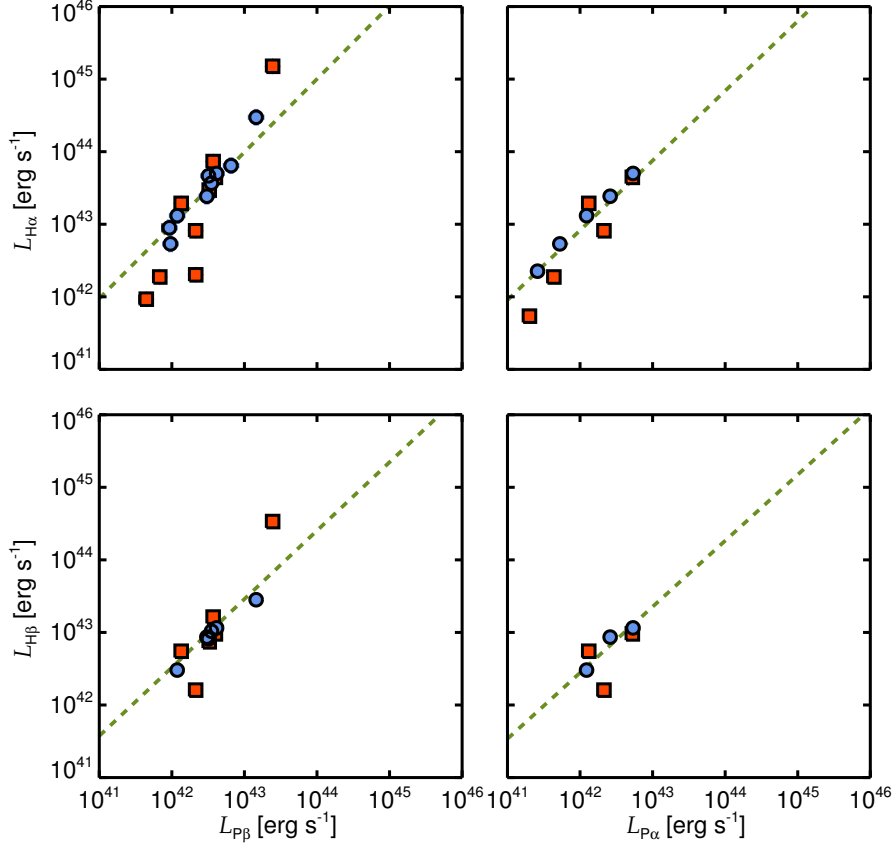


FIG. 7.— Observed and dust-extinction-corrected line luminosities of NIR-red AGNs. The red squares show the observed line luminosities, and the blue circles mean the dust-extinction-corrected line luminosities with the measured $E(B - V)_{\text{line}}$ values. The green dotted lines represent the correlations between the Balmer and Paschen line luminosities (Kim et al. 2010), and these correlations are used for estimating the $E(B - V)_{\text{line}}$ values.

we measure different types of Balmer-decrement-based $E(B - V)$ values (hereafter, $E(B - V)_{\text{BD2}}$). First, we combine two relations of $L_{\text{H}\alpha}$ - $L_{\text{P}\alpha}$ and $L_{\text{H}\beta}$ - $L_{\text{P}\alpha}$ from Kim et al. (2010) to make a relation of $L_{\text{H}\alpha}$ - $L_{\text{H}\beta}$. The combined relation is

$$\log \left(\frac{L_{\text{H}\alpha}}{10^{42} \text{ erg s}^{-1}} \right) = 0.509 + 1.056 \log \left(\frac{L_{\text{H}\beta}}{10^{42} \text{ erg s}^{-1}} \right) \quad (6)$$

that is used as the intrinsic $L_{\text{H}\alpha}$ - $L_{\text{H}\beta}$ relation of NIR-red AGNs. Second, we measure the $E(B - V)_{\text{BD2}}$ values by varying the amount of dust-reddening to minimize χ^2 , which is a function of the $L_{\text{H}\alpha}/L_{\text{H}\beta}$ of NIR-red AGNs (R_{obs}) and unobscured type 1 quasars (R_{int}), expressed as

$$\chi^2 = \frac{(R_{\text{obs}} - E(R_{\text{int}}))^2}{\sigma^2}. \quad (7)$$

Here, the R_{int} is derived from the above relation of $L_{\text{H}\alpha}$ - $L_{\text{H}\beta}$, E is a dust-reddening function, and σ is the combined uncertainty of the R_{obs} and R_{int} . The measured $E(B - V)_{\text{BD2}}$ values are summarized in Table 7.

The $E(B - V)_{\text{BD2}}$ values show tighter correlations with the $E(B - V)_{\text{line}}$ and $E(B - V)_{\text{cont}}$ values than the $E(B - V)_{\text{BD1}}$ values, but these comparisons cannot be meaningful due to the small number statistics. The comparisons of the $E(B - V)_{\text{BD2}}$ values with the $E(B - V)_{\text{line}}$

and $E(B - V)_{\text{cont}}$ values are shown in Figure 10. Between the $E(B - V)_{\text{BD2}}$ and $E(B - V)_{\text{line}}$ values, the Pearson correlation coefficient is 0.816, with an rms scatter of 0.249. For the $E(B - V)_{\text{BD2}}$ and $E(B - V)_{\text{cont}}$ values, the Pearson correlation coefficient and the rms scatter are 0.941 and 0.136, respectively. These Pearson correlation coefficients are significantly bigger than the coefficients from the $E(B - V)_{\text{BD1}}$ values.

Although the difference cannot be meaningful due to the small number statistics, if there is a difference, we suspect the different intrinsic $L_{\text{H}\alpha}/L_{\text{H}\beta}$ causes these conflicting results. Because the intrinsic Balmer decrements are fixed to 4.526 for deriving the $E(B - V)_{\text{BD1}}$ values, these quantities vary with the $L_{\text{H}\beta}$ values for the $E(B - V)_{\text{BD2}}$ values. For example, when the $L_{\text{H}\beta}$ is increased from $10^{42} \text{ erg s}^{-1}$ to $10^{44} \text{ erg s}^{-1}$, the intrinsic Balmer decrement increases from 3.23 to 4.18, which makes up $\sim 22\%$ of the discrepancy of the measured $E(B - V)$ values.

4.4. Color selection for dusty red AGNs

In Urrutia et al. (2009), their red AGNs were classified to have $E(B - V) > 0.1$. Only two objects among the ~ 50 candidates in Urrutia et al. (2009) have $E(B - V) < 0.1$, and these two were not classified as dusty red AGNs. In this study, considering the rms scatter of the $E(B - V)$ values, $E(B - V) \sim 0.2$ is virtually identical to no extinc-

TABLE 7
FOUR KINDS OF $E(B - V)$ VALUES

Object	$E(B - V)_{\text{line}}$ (mag)	$E(B - V)_{\text{cont}}$ (mag)	$E(B - V)_{\text{BD1}}$ (mag)	$E(B - V)_{\text{BD2}}$ (mag)
0106+2603	—	0.675±0.001	0.137±0.005	0.371±0.005
0157+1712	1.596±0.034	2.157±0.008	—	—
0221+1327	0.484±0.032	0.990±0.008	—	—
0234+2438	—	—	—	—
0324+1748	-0.745±0.007	-0.026±0.000	-0.013±0.004	-0.003±0.004
0348+1255	—	1.326±0.010	—	—
1258+2329	-0.179±0.021	0.091±0.001	-0.213±0.027	-0.006±0.023
1307+2338	—	—	—	—
1453+1353	0.657±0.060	0.890±0.002	—	—
1543+1937	0.057±0.013	0.169±0.000	0.020±0.004	0.175±0.004
1659+1834	0.505±0.007	0.636±0.001	0.096±0.014	0.315±0.012
2222+1952	—	—	—	—
2222+1959	-0.208±0.008	0.271±0.000	-0.007±0.003	0.129±0.002
2303+1624	—	—	—	—
2327+1624	1.043±0.154	0.681±0.003	—	—
2344+1221	0.101±0.008	0.259±0.000	-0.109±0.004	0.073±0.004

tion, and we classify the objects with $E(B - V) > 0.2$ as dusty red AGNs. According to this criteria, among our sample, three (0324+1748, 1258+2329, and 1543+1937) or five (0324+1748, 1258+2329, 1543+1937, 2222+1959, and 2344+1221) objects cannot be classified as dusty red AGNs based on the $E(B - V)_{\text{cont}}$ or $E(B - V)_{\text{line}}$ values, respectively, and the fraction of the low- $E(B - V)$ red AGNs (LERA) is bigger than that of Urrutia et al. (2009).

To figure out why this discrepancy arises, we check the differences in sample selection for the two studies. In order to select the red AGN candidates, Urrutia et al. (2009) used the optical-NIR ($r' - K > 5$) and NIR colors ($J - K > 1.3$) of FIRST-detected objects, but our sample was selected by NIR color only ($J - K > 2$). Our entire sample within the FIRST coverage has detections in this survey, so the difference in the LERA fraction of the two samples originates from the lack of the optical-NIR color selection, and the NIR color alone is not sufficient to select dusty red AGNs. As shown in Figure 11, the change in $E(B - V)$ due to the increase in $J - K$ is not significant, but the $E(B - V)$ values are larger ($E(B - V) > 0$) when $g' - K > 5$. Moreover, this result is supported by Maddox & Hewett (2006), in which a significant fraction of unobscured type 1 AGNs at low redshifts have such an NIR color of $J - K > 2$. We conclude that a significant portion of the NIR-red AGNs is unobscured or only mildly obscured type 1 AGNs.

5. ACCRETION RATES

In this section, we measure the λ_{Edd} ($L_{\text{bol}}/L_{\text{Edd}}$, where L_{Edd} is the Eddington luminosity) of NIR-red AGNs at $z \sim 0.3$. To obtain the quantities, we derive BH masses and bolometric luminosities after correcting for the dust extinction by using the $E(B - V)_{\text{line}}$ values to avoid the effects of dust extinction. If the taken $E(B - V)_{\text{line}}$ is negative, we did not correct the dust extinction under an assumption that there is no dust extinction.

As a comparison sample, we use the unobscured type 1 quasars in the quasar property catalog (Shen et al. 2011) of the SDSS Seventh Data Release (DR7; Abazajian et al. 2009). To avoid the effects of sample bias, we set the sample selection criteria to be identical to those of our NIR-red AGNs: (i) $0.139 \leq z \leq 0.411$ and (ii) detec-

tion in all three 2MASS bands. Finally, we select 4130 unobscured type 1 quasars through the sample selection criteria.

Considering that the λ_{Edd} values may have dependence on the L_{bol} values (e.g., Lusso et al. 2012; Suh et al. 2015), these selected control samples may cause the sample bias effects. Thus, we address this issue in Section 5.3 by placing restraints on these samples with limited ranges of the L_{bol} and M_{BH} .

5.1. BH masses

In order to measure the BH masses of NIR-red AGNs, NIR M_{BH} estimators (e.g., Kim et al. 2010, 2015a; Landt et al. 2011b) are used to alleviate the effects of the dust extinction. We adopt the Paschen-line-based M_{BH} estimators (Kim et al. 2010, 2015b), to which we applied a recent virial coefficient of $\log f = 0.05$ (Woo et al. 2015). Note that the virial factor, f , is the proportional coefficient that is needed to determine the BH mass based on the virial theorem:

$$M_{\text{BH}} = f \frac{R \Delta V^2}{G}, \quad (8)$$

where R is the BLR size, ΔV is the velocity of the BLR gas, and G is the gravitational constant. The value of $\log f = 0.05$ (Woo et al. 2015) is for the case of ΔV being the FWHM of the line. If the line dispersion is used for ΔV , the $\log f$ value is different. The modified, new virial-coefficient-applied, Paschen-line-based M_{BH} estimators are

$$\frac{M_{\text{BH}}}{M_{\odot}} = 10^{7.04 \pm 0.02} \left(\frac{L_{\text{P}\beta}}{10^{42} \text{ erg s}^{-1}} \right)^{0.48 \pm 0.03} \left(\frac{\text{FWHM}_{\text{P}\beta}}{10^3 \text{ km s}^{-1}} \right)^2 \quad (9)$$

and

$$\frac{M_{\text{BH}}}{M_{\odot}} = 10^{7.07 \pm 0.04} \left(\frac{L_{\text{P}\alpha}}{10^{42} \text{ erg s}^{-1}} \right)^{0.49 \pm 0.06} \left(\frac{\text{FWHM}_{\text{P}\alpha}}{10^3 \text{ km s}^{-1}} \right)^2. \quad (10)$$

We measure the BH masses for 11 and 6 NIR-red AGNs by using the P β - and P α -based M_{BH} estimators, respectively. There is no significant difference between the measured P β - and P α -based BH masses as shown in Figure 12, and the measured BH masses are listed in Table 8.

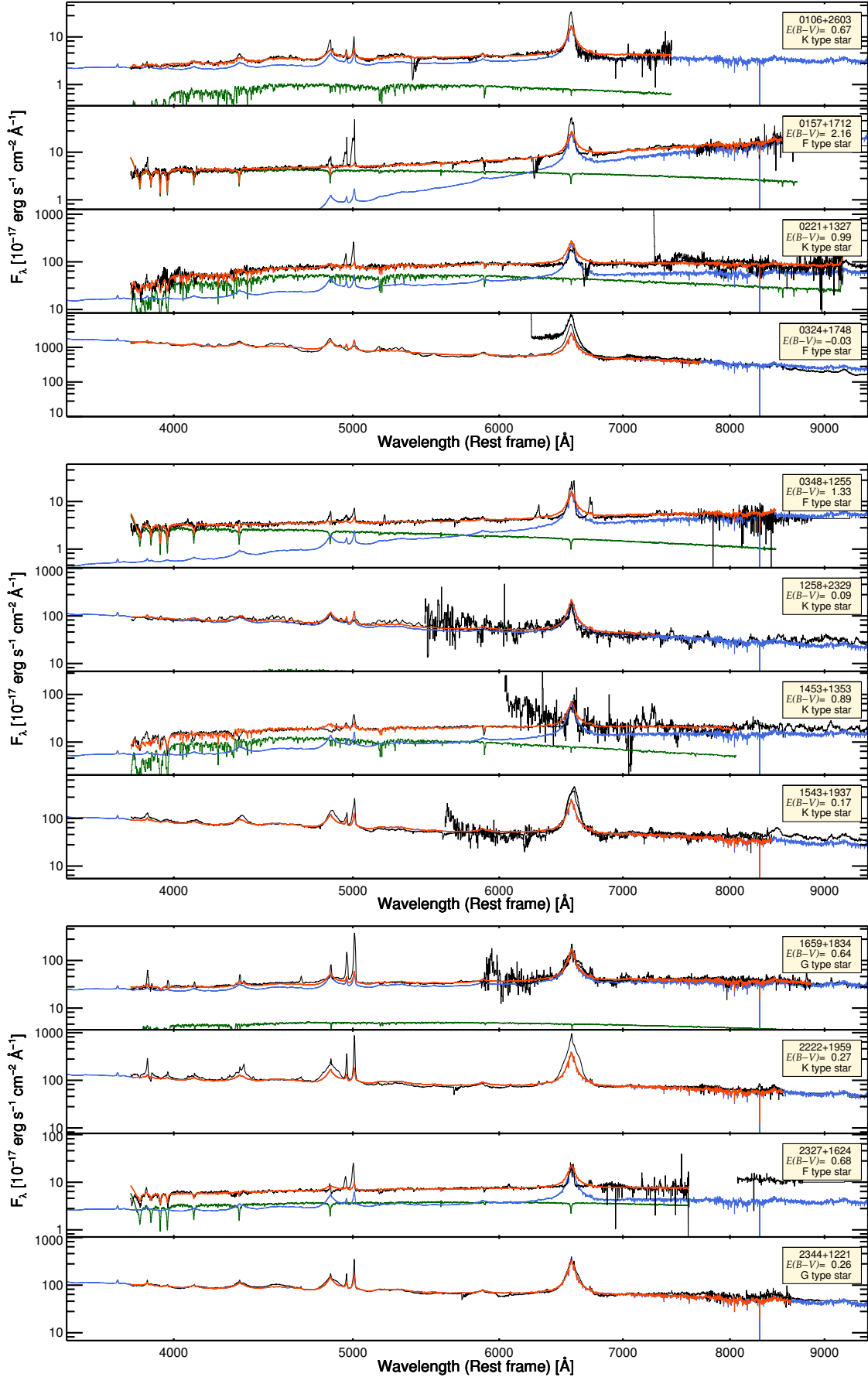


FIG. 8.— Spectra of NIR-red AGNs with the best-fit models are shown in the rest-frame from 3790 to 10000 Å. The black lines denote the observed spectra. The green and blue lines are the best-fit model stellar and quasar spectra, respectively, that also include the dust-reddening. The red line shows the sum of the best-fit stellar and quasar spectra. The top right box denotes the name of NIR-red AGN, the measured $E(B-V)_{\text{cont}}$, and the used stellar template. Note that the host galaxy dominates the spectra of 0157+1712, 0221+1327, and 0348+1255 at short wavelength range (< 6500 Å) due to heavy extinction of the AGN component.

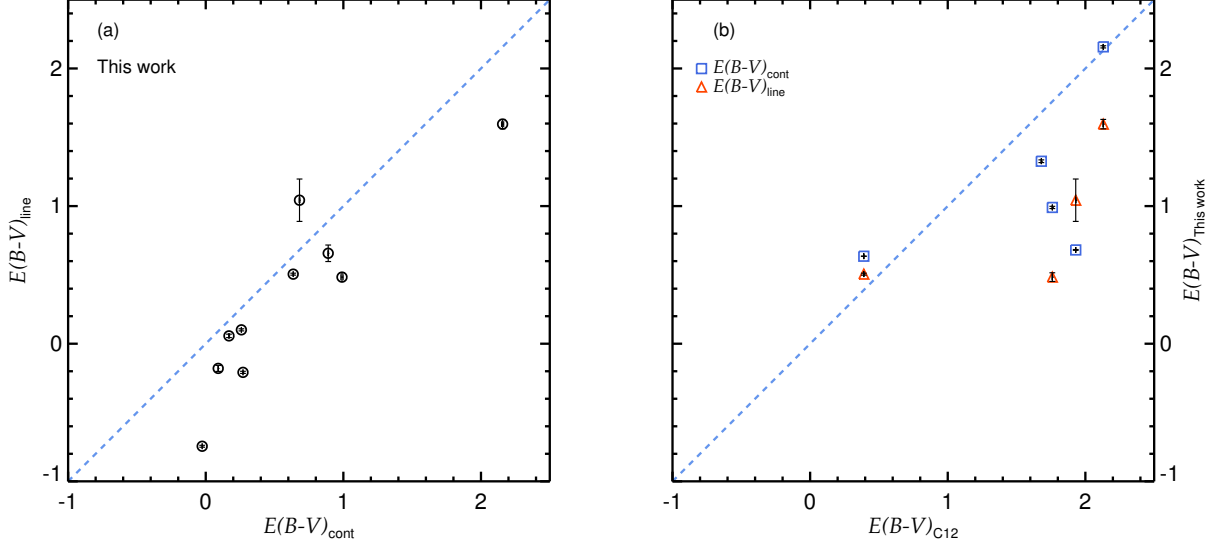


FIG. 9.— (a) Comparison between the $E(B-V)_{\text{line}}$ values and the $E(B-V)_{\text{cont}}$ values of NIR-red AGNs. The blue dashed line denotes a line where the two values are identical. (b) We compare the two types of $E(B-V)$ values with the $E(B-V)_{\text{C12}}$ values. The blue squares and red triangles represent the $E(B-V)_{\text{cont}}$ and $E(B-V)_{\text{line}}$ values, respectively. The meaning of the blue dashed line is identical to that of the left panel.

To obtain the BH masses of unobscured type 1 quasars, we use an optical M_{BH} estimator (McLure & Dunlop 2004) consisting of λL_{5100} (L5100) and $\text{FWHM}_{\text{H}\beta}$. For the optical M_{BH} estimator, we apply the virial coefficient of Woo et al. (2015) as

$$\frac{M_{\text{BH}}}{M_{\odot}} = 5.27 \left(\frac{L_{5100}}{10^{44} \text{ erg s}^{-1}} \right)^{0.61} \left(\frac{\text{FWHM}_{\text{H}\beta}}{\text{km s}^{-1}} \right)^2. \quad (11)$$

The L5100 and $\text{FWHM}_{\text{H}\beta}$ values of unobscured type 1 quasars are adopted from Shen et al. (2011).

5.2. Bolometric luminosities

To estimate the bolometric luminosities of NIR-red AGNs, we combine several empirical relations between the bolometric luminosity (L_{bol}), the continuum luminosity, and the line luminosity. We bootstrap the empirical relations between L_{bol} and L5100 (Shen et al. 2011), L5100 and $L_{\text{H}\alpha}$ (Jun et al. 2015), and $L_{\text{H}\alpha}$ and the two Paschen line luminosities (Kim et al. 2010). The combined relations between L_{bol} and the Paschen line luminosities are

$$\log \left(\frac{L_{\text{bol}}}{10^{44} \text{ erg s}^{-1}} \right) = 1.33 + 0.966 \log \left(\frac{L_{\text{P}\beta}}{10^{42} \text{ erg s}^{-1}} \right) \quad (12)$$

and

$$\log \left(\frac{L_{\text{bol}}}{10^{44} \text{ erg s}^{-1}} \right) = 1.27 + 0.920 \log \left(\frac{L_{\text{P}\alpha}}{10^{42} \text{ erg s}^{-1}} \right). \quad (13)$$

We measured the L_{bol} values for 12 and 6 NIR-red AGNs by using $L_{\text{P}\beta}$ and $L_{\text{P}\alpha}$, respectively. The L_{bol} measured from $\text{P}\beta$ and $\text{P}\alpha$ show no significant differences, as shown in Figure 12, and the measured L_{bol} values are listed in Table 8.

To obtain the L_{bol} values of unobscured type 1 quasars, we use L5100 values, with the bolometric correction factor (9.26) for L5100, both of which are adopted from

Shen et al. (2011).

5.3. Eddington ratios of NIR-red AGNs

When comparing the λ_{Edd} values of NIR-red AGNs to those of unobscured type 1 quasars, we prefer to use the λ_{Edd} values from $\text{P}\alpha$ than those from $\text{P}\beta$ when both quantities are available, to minimize the effects from the dust extinction. The λ_{Edd} values of nine NIR-red AGNs are used for the comparison, among which four (0157+1712, 0324+1748, 2222+1959, and 2344+1221) and five (0221+1327, 1258+2329, 1453+1353, 1543+1937, and 1659+1834) λ_{Edd} values are derived from $\text{P}\beta$ and $\text{P}\alpha$, respectively.

The M_{BH} and L_{bol} values of NIR-red AGNs and unobscured type 1 quasars are shown in Figure 13, and Figure 14 shows their distributions of λ_{Edd} values. We find that the median λ_{Edd} of the nine NIR-red AGNs, $\log(\lambda_{\text{Edd}}) = -0.654 \pm 0.174$, where the error represents the error of the median, is only mildly higher than that of unobscured type 1 quasars, $\log(\lambda_{\text{Edd}}) = -0.961 \pm 0.008$. For quantifying how significantly these two distributions of the λ_{Edd} values differ from each other, we perform the Kolmogorov-Smirnov test (K-S test) by using the KSTW0 code based on IDL. The maximum deviation between the cumulative distributions of these two λ_{Edd} values, D , is 0.392, and the probability of the result given the null hypothesis, p , is 0.094.

From this comparison, we conclude that the λ_{Edd} of the NIR-red AGNs is only slightly larger than that of the unobscured type 1 AGNs, but statistically the difference is not significant. A few outliers with large λ_{Edd} appear to dominate the K-S test result, and this suggests that the NIR-red AGN sample is mostly indiscernible in their property from unobscured type 1 AGNs, but can include truly dusty high λ_{Edd} AGNs such as 0157+1712 with $E(B-V)_{\text{line}} = 1.596$.

Since λ_{Edd} values can depend on the L_{bol} values (e.g., Lusso et al. 2012; Suh et al. 2015), we repeated the anal-

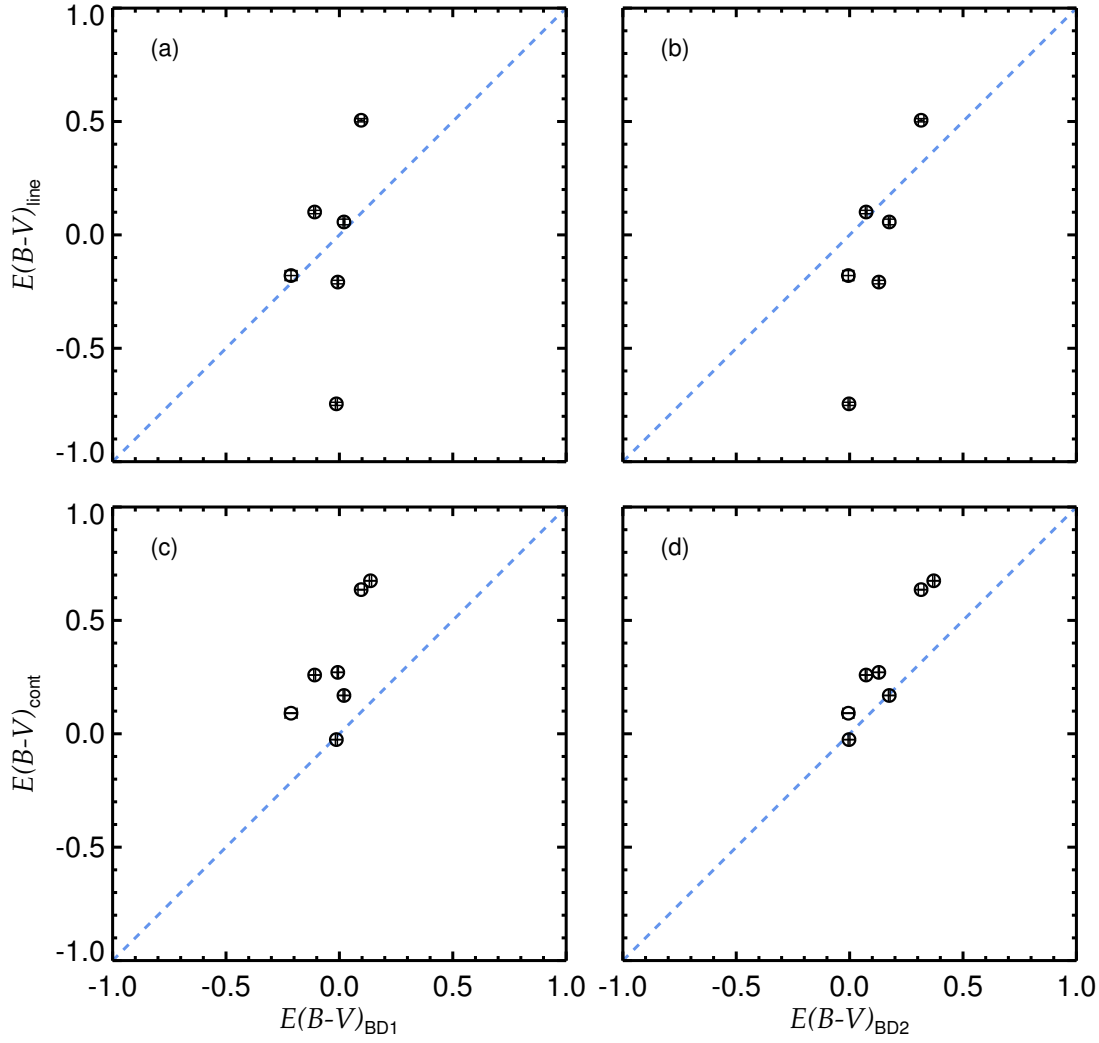


FIG. 10.— (a) Comparison between the $E(B-V)_{\text{BD1}}$ and the $E(B-V)_{\text{line}}$ values of NIR-red AGNs. The meaning of the blue dashed line is identical to Figure 9. (b) The $E(B-V)_{\text{BD2}}$ vs. $E(B-V)_{\text{line}}$ values. (c) The $E(B-V)_{\text{BD1}}$ vs. $E(B-V)_{\text{cont}}$ values. (d) The $E(B-V)_{\text{BD2}}$ vs. $E(B-V)_{\text{cont}}$ values.

ysis after matching their L_{bol} values. First, we divide the NIR-red AGNs into two sub-samples, four low- L_{bol} (0221+1327, 1258+2329, 1453+1353, and 1659+1834; $44.73 \leq \log(L_{\text{bol}}/\text{erg s}^{-1}) \leq 45.65$) and five high- L_{bol} (0157+1712, 0324+1748, 1543+1937, 2222+1959, and 2344+1221; $45.86 \leq \log(L_{\text{bol}}/\text{erg s}^{-1}) \leq 46.67$) NIR-red AGNs. Second, among all the unobscured type 1 AGNs, we choose 3688 low- L_{bol} ($44.76 \leq \log(L_{\text{bol}}/\text{erg s}^{-1}) \leq 45.65$) and 165 high- L_{bol} ($45.86 \leq \log(L_{\text{bol}}/\text{erg s}^{-1}) \leq 46.55$) sub-samples that have the similar L_{bol} ranges to those of the divided NIR-red AGNs.

By comparing such the L_{bol} limited samples, we confirm the result from the full sample, which is the λ_{Edd} of NIR-red AGNs is only mildly higher than that of unobscured type 1 AGNs. For the low- L_{bol} samples, the median $\log(\lambda_{\text{Edd}})$ values of the NIR-red AGNs and unobscured type 1 AGNs are -0.654 ± 0.216 and -0.995 ± 0.008 , respectively. For the high- L_{bol} samples, although the λ_{Edd} values are larger than those of the low- L_{bol} sam-

ples, the result is consistent throughout. The median $\log(\lambda_{\text{Edd}})$ of the NIR-red AGNs is -0.424 ± 0.276 , and that of the unobscured type 1 AGNs is -0.661 ± 0.035 .

We also compare the λ_{Edd} of unobscured type 1 quasars to those of NIR-red AGNs with $E(B-V) > 0.2$. The comparison is shown in Figure 14. We find that the median $\log(\lambda_{\text{Edd}})$ of the NIR-red AGNs is -0.654 ± 0.321 , which is consistent with the above results.

6. $M_{\text{BH}}-\sigma_*$ RELATION

In this section, we discuss the $M_{\text{BH}}-\sigma_*$ relation of NIR-red AGNs. For the relation, we adopt the σ_* values from Canalizo et al. (2012) which are measured using the stellar absorption lines in the range of 3900–5500 Å. However, the σ_* values are available for only three objects (0157+1712, 0221+1327, and 1659+1834) in our sample. These three NIR-red AGNs have $E(B-V) > 0.2$.

For the BH masses, Canalizo et al. (2012) also estimated the BH masses using the L5100 and $\text{FWHM}_{\text{H}\alpha}$

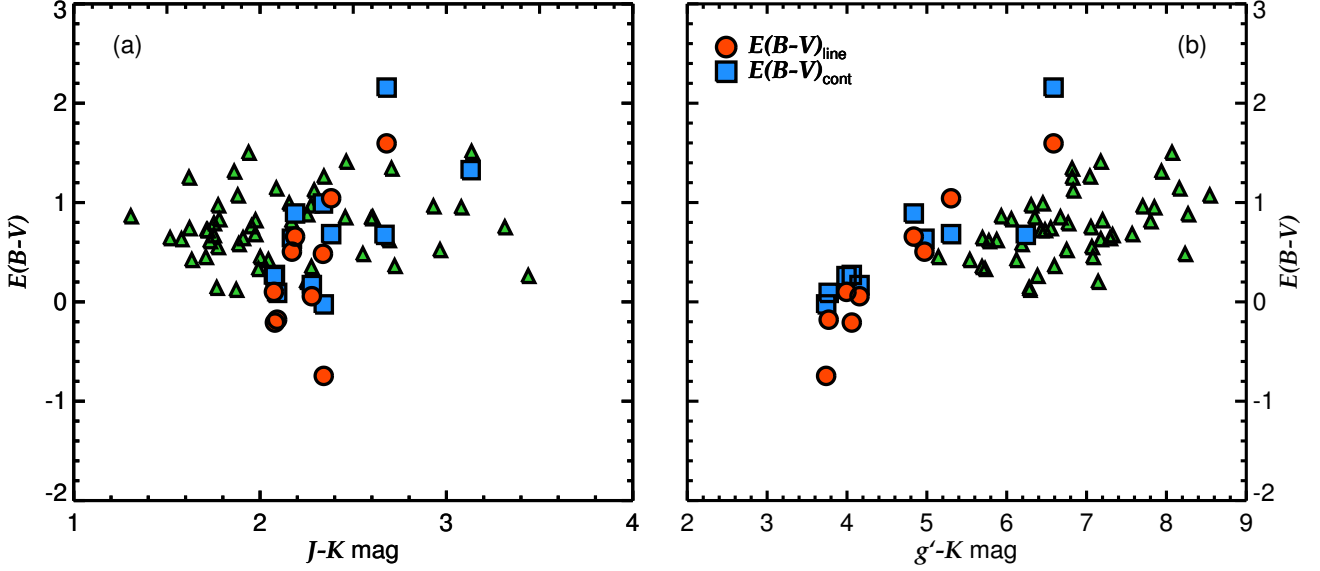


FIG. 11.— (a) Comparison between the measured $E(B - V)$ values and $J - K$ magnitudes. The blue squares and red circles represent that the $E(B - V)$ values are the $E(B - V)_{\text{cont}}$ and $E(B - V)_{\text{line}}$ values, respectively. The green triangles show the $J - K$ and $E(B - V)$ values of the red quasars in Urrutia et al. (2009). (b) Comparison of $g' - K$ magnitudes vs. the $E(B - V)$ values. The meanings of the blue squares, red circles, and green triangles are identical to those of the left panel.

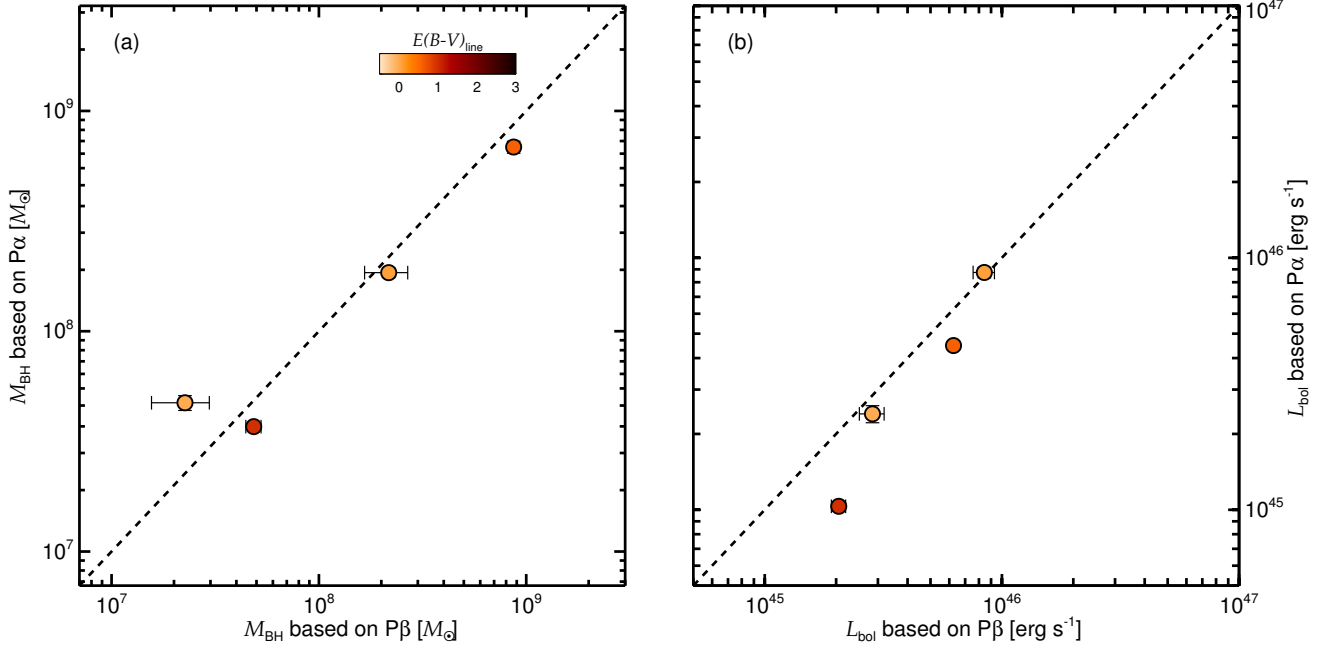


FIG. 12.— (a) Comparison between the measured M_{BH} based on $P\beta$ and $P\alpha$ lines. The BH masses are represented by circles, and the colors in the circles mean their $E(B - V)_{\text{line}}$ values. (b) Comparison of the L_{bol} values derived from $P\beta$ vs. $P\alpha$ lines. The circles denote the L_{bol} values, and the meaning of the colors in the circles is identical to the left panel.

values, but we use the Paschen-line-based BH masses measured in Section 5.2. We compare these two kinds of BH masses. In Canalizo et al. (2012), the BH masses based on L5100 and $\text{FWHM}_{\text{H}\alpha}$ are $10^{8.35}$, $10^{8.42}$, and $10^{8.68} M_{\odot}$ for 0157+1712, 0221+1327, and 1659+1834, respectively, whereas the BH masses derived from the Paschen lines are $10^{7.96}$, $10^{7.57}$, and $10^{8.84} M_{\odot}$. Although there is no significant difference in the BH masses for 0157+1712 and 1659+1834, the Paschen-line-based BH mass of 0221+1327 is smaller by a factor of ~ 7 . The dis-

crepancy for the BH mass of 0221+1327 does not come from the dust extinction but from the spectral line fitting. In Canalizo et al. (2012), they measured the FWHM as 4279 km s^{-1} , which is estimated from the $\text{H}\alpha$ line. In this study, we measured the FWHM from the $\text{H}\alpha$, $P\beta$, and $P\alpha$ lines, which gives 2212 , 2125 , and 2073 km s^{-1} , respectively, and these values are significantly smaller than the previous result.

In Figure 15, the newly established $M_{\text{BH}} - \sigma_*$ relation of NIR-red AGNs is presented, along with those for local

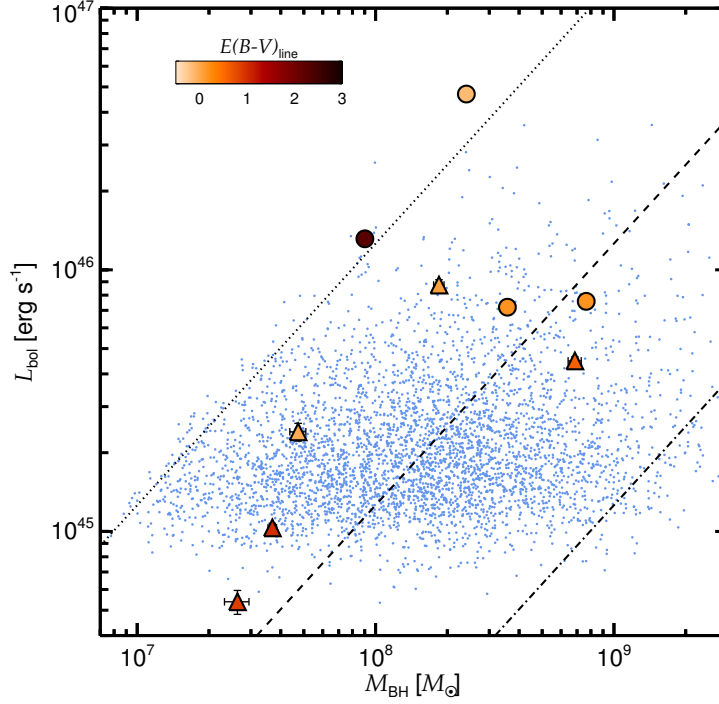


FIG. 13.— The L_{bol} and M_{BH} values of NIR-red AGNs and unobscured type 1 quasars. The circles and triangles show the L_{bol} and M_{BH} values of NIR-red AGNs derived from $P\beta$ and $P\alpha$, respectively. The meaning of the colors in the circles and triangles is identical to that in Figure 12. The blue dots represent the L_{bol} and M_{BH} values of unobscured type 1 quasars. The dotted, dashed, and dash-dotted lines denote λ_{Edd} of 1, 0.1, and 0.01, respectively.

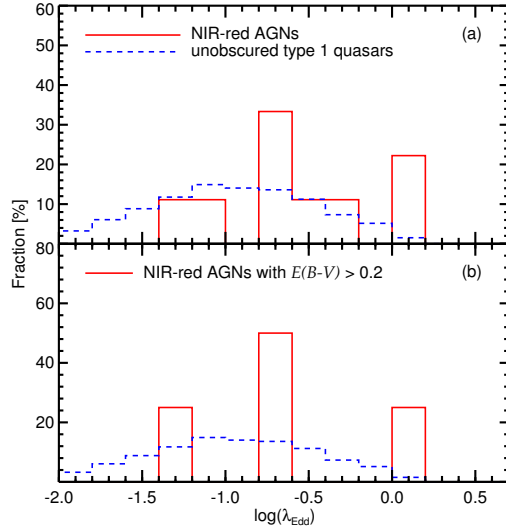


FIG. 14.— (a) Distributions of the λ_{Edd} values of NIR-red AGNs and unobscured type 1 quasars. The red solid and blue dashed histograms show the λ_{Edd} distributions of NIR-red AGNs and unobscured type 1 quasars, respectively. (b) Distributions of the λ_{Edd} of NIR-red AGNs with $E(B-V) > 0.2$ and unobscured type 1 quasars. The meaning of the red solid lines, blue dashed lines, and the ranges of the L_{bol} and M_{BH} are identical to those in panel (a).

quiescent galaxies (Gültekin et al. 2009) and unobscured type 1 AGNs at $z \simeq 0, 0.36, 0.57$, and $\lesssim 1$ (Woo et al. 2006, 2008, 2010; Shen et al. 2015). These $M_{\text{BH}}-\sigma_*$ relations of unobscured type 1 AGNs are modified by applying the virial coefficient of $\log f = 0.05$ (Woo et al. 2015), as we did for NIR-red AGNs.

By comparing the $M_{\text{BH}}-\sigma_*$ relation of NIR-red AGNs and local unobscured type 1 AGNs (Woo et al. 2010), we find offsets of $\Delta \log(M_{\text{BH}}/M_\odot) = -0.389, 0.243$, and 1.190 for 0157+1712, 0221+1327, and 1659+1834, respectively, resulting in a mean offset of $\Delta \log(M_{\text{BH}}/M_\odot) = 0.348 \pm 0.902$. The $M_{\text{BH}}-\sigma_*$ relation for NIR-red AGNs and those for unobscured type 1 AGNs at $z = 0$ through 0.5 are consistent with each other (e.g., $\Delta \log(M_{\text{BH}}/M_\odot) = 0.74, 0.62$, and 0.52 for unobscured type 1 AGNs at $z = 0.26, 0.36$, and 0.57 , respectively; Shen et al. 2015; Woo et al. 2006, 2008). This result suggests that there is no significant offset in the $M_{\text{BH}}-\sigma_*$ relation between the NIR-red AGNs and the unobscured type 1 AGNs, although more objects are needed to better quantify the offset.

Moreover, we compare the $M_{\text{BH}}-\sigma_*$ relations of NIR-red AGNs and unobscured type 1 AGNs after matching their L_{bol} values to exclude the selection bias introduced from their different luminosities (e.g., Shen et al. 2015). The L_{bol} values of 0157+1712, 0221+1327, and 1659+1834 are $10^{46.12}$, $10^{45.01}$, and $10^{45.65} \text{ erg s}^{-1}$, respectively, as shown in Figure 16, and the L_{bol} values of the unobscured type 1 AGNs at $z \simeq 0.36$ (Woo et al. 2006), 0.57 (Woo et al. 2008), and $\lesssim 1$ (Shen et al. 2015) are measured by applying the bolometric correction factor of 9.26 (Shen et al. 2011) to their L5100 values. Among them, we choose 42 unobscured type 1 AGNs that have similar, but somewhat lower, L_{bol} range ($10^{45.01} \leq L_{\text{bol}}/\text{erg s}^{-1} \leq 10^{45.73}$), to that of the NIR-red AGNs. For the selected unobscured type 1 AGNs, their

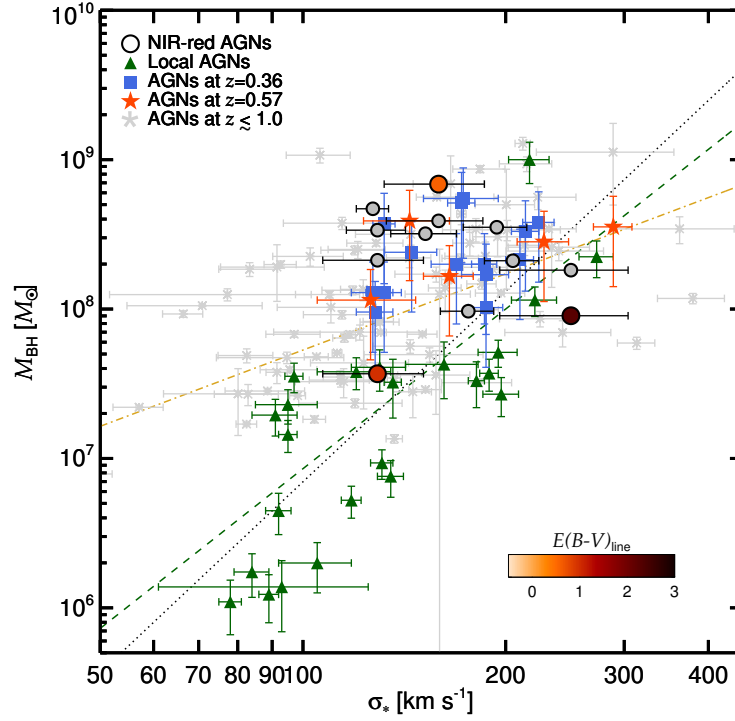


FIG. 15.— $M_{\text{BH}}-\sigma_*$ relations of AGNs. Circles denote the M_{BH} and σ_* values of NIR-red AGNs, and the meaning of the colors in the circles is identical to Figure 11. The gray circles denote the quantities of NIR-red AGNs measured in Canalizo et al. (2012). The M_{BH} and σ_* values of unobscured type 1 AGNs at $z \simeq 0$ (Woo et al. 2010), 0.36 (Woo et al. 2006), 0.57 (Woo et al. 2008), and $\lesssim 1$ (Shen et al. 2015) are represented by green triangles, blue squares, red stars, and gray asterisks, respectively. The green dashed, black dotted, and yellow dot-dashed lines show the $M_{\text{BH}}-\sigma_*$ relations for local AGNs (Woo et al. 2010), quiescent local galaxies (Gültekin et al. 2009), and unobscured type 1 AGNs at $z \sim 0.26$ (Shen et al. 2015).

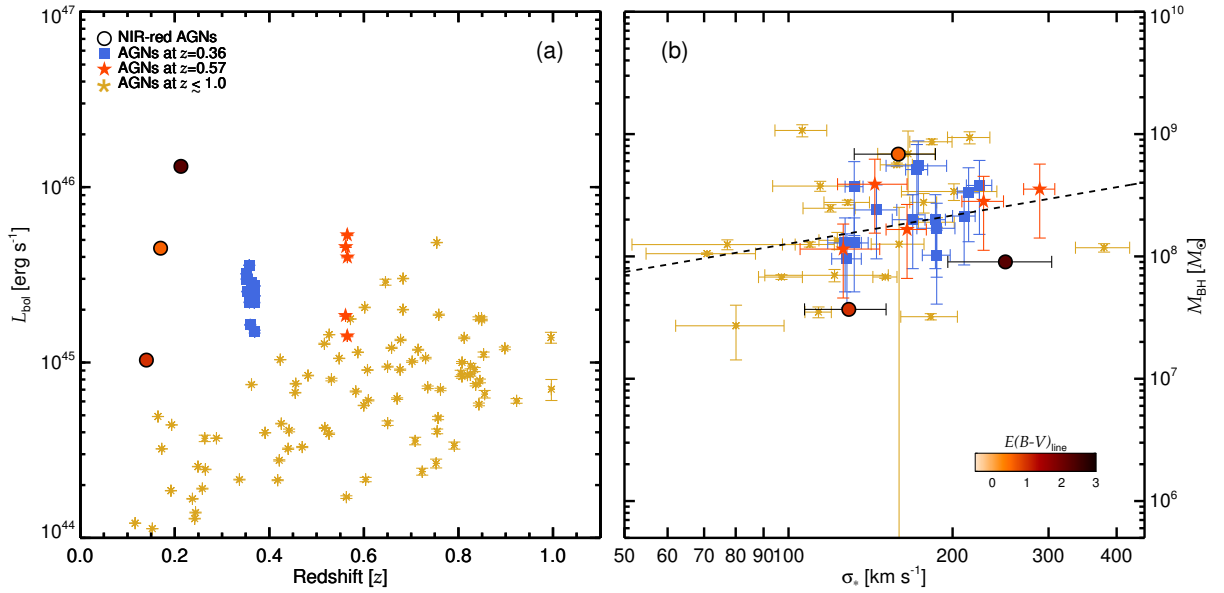


FIG. 16.— (a) The L_{bol} values vs. redshifts of NIR-red AGNs and unobscured type 1 AGNs. The circles denote the redshifts and L_{bol} values of NIR-red AGNs, and the meaning of the colors in the circles is identical to those in Figure 11. The blue squares, red stars, and yellow asterisks represent the quantities of unobscured type 1 AGNs at $z \simeq 0.36$ (Woo et al. 2006), 0.57 (Woo et al. 2008), and $\lesssim 1$ (Shen et al. 2015), respectively. (b) $M_{\text{BH}}-\sigma_*$ relations of the luminosity-matched AGNs. The meaning of circles, blue squares, red stars, and yellow asterisks have meanings identical to those in the left panel. The black dashed line indicates the $M_{\text{BH}}-\sigma_*$ relation of the luminosity-matched unobscured type 1 AGNs, where the measured α and β are 8.335 ± 0.016 and 0.768 ± 0.083 , respectively.

M_{BH} can be expressed as a function of σ_* :

$$\log\left(\frac{M_{\text{BH}}}{M_{\odot}}\right) = \alpha + \beta \log\left(\frac{\sigma_*}{200 \text{ km s}^{-1}}\right), \quad (14)$$

and the measured α and β are 8.335 ± 0.016 and 0.768 ± 0.083 , respectively. By comparing the newly measured $M_{\text{BH}}-\sigma_*$ relation of the unobscured type 1 AGNs and that of the NIR-red AGNs, we find a mean offset of $\Delta \log(M_{\text{BH}}/M_{\odot}) = -0.166 \pm 0.681$, as presented in Figure 16. In this luminosity-matched comparison, the number of the NIR-red AGNs is also insufficient, but we obtain the same result that there is no significant offset between the $M_{\text{BH}}-\sigma_*$ relations of the NIR-red AGNs and the unobscured type 1 AGNs.

7. SUMMARY

By performing NIR spectroscopic observations with four telescopes, Gemini, IRTF, Magellan, and Subaru, we obtained 0.7–2.5 μm medium-resolution ($R > 2000$) and high-S/N (up to several hundreds) spectra of 16 NIR-red AGNs at $z \sim 0.3$. In addition to the NIR spectra, we obtained optical (0.4–1.0 μm) medium-resolution ($R \sim 4000$) spectra of 12 NIR-red AGNs taken with Keck/ESI and SDSS data. Using both sets of spectra, we measured the line luminosities and FWHMs of H β , H α , P β , and P α lines for 7, 12, 12, and 6 NIR-red AGNs, respectively.

Before analyzing the physical properties of NIR-red AGNs, we derived the $E(B-V)$ values of NIR-red AGNs in two ways. First, we estimated the $E(B-V)_{\text{line}}$ values by using the luminosity ratios of H β , H α , P β , and P α lines. Second, the $E(B-V)_{\text{cont}}$ values were measured by comparing the continuum slopes at 3790–10000 Å. Through these two methods, we measured the $E(B-V)_{\text{line}}$ and $E(B-V)_{\text{cont}}$ values for 10 and 12 NIR-red AGNs, respectively. These two $E(B-V)$ values are consistent, and their Pearson correlation coefficient is 0.911.

Among our sample, five objects have low $E(B-V) < 0.2$. Comparing the previous result (Urrutia et al. 2009) from the optical-NIR and NIR color selection that yields

only two objects have low $E(B-V)$ values in ~ 50 candidates, we suspect that the NIR red color selection alone is not effective at picking up dusty red AGNs.

After correcting for the dust extinction with the measured $E(B-V)$ values, we measured the λ_{Edd} values of NIR-red AGNs. For the M_{BH} and L_{bol} values, we used Paschen-line-based M_{BH} and L_{bol} estimators to alleviate the effects of the dust extinction. The newly estimated median λ_{Edd} of NIR-red AGNs, $\log(\text{Edd}) = -0.654 \pm 0.174$, is only mildly higher than that of unobscured type 1 quasars, $\log(\text{Edd}) = -0.961 \pm 0.008$.

Using the measured BH masses, we compared the $M_{\text{BH}}-\sigma_*$ relation of NIR-red AGNs to that of unobscured type 1 AGNs at similar redshift. Although only three objects were used, NIR-red AGNs show a tendency to have similar BH masses at a fixed the σ_* .

Our results suggest that AGNs with red $J-K$ colors are not necessarily dust-obscured AGNs, and the selection of dusty AGNs needs to be carefully performed.

We thank the referee for useful comments. This work was supported by the Creative Initiative Program of the National Research Foundation of Korea (NRF), No. 2017R1A3A3001362, funded by the Korea government (MSIP). D.K. acknowledges support by the National Research Foundation of Korea to the Fostering Core Leaders of the Future Basic Science Program, No. 2017-002533. The Gemini data were taken through the K-GMT Science Program (PID: GN-2015B-Q-51; GN-2016A-Q-86) of Korea Astronomy and Space Science Institute (KASI). This paper includes data obtained with the 6.5 m Magellan Telescopes located at Las Campanas Observatory, Chile. D.K. and M.I. are Visiting Astronomers (PID: 2015B092; 2016A043) at the Infrared Telescope Facility, which is operated by the University of Hawaii under Cooperative Agreement no. NNX-08AE38A with the National Aeronautics and Space Administration, Science Mission Directorate, Planetary Astronomy Program. This paper includes data obtained with Subaru telescope and W. M. Keck observatory on Maunakea.

REFERENCES

- Abazajian, K. N., Adelman-McCarthy, J. K., Agüeros, M. A., et al. 2009, *ApJS*, 182, 543
- Anderson, S. F., Voges, W., Margon, B., et al. 2003, *AJ*, 126, 2209
- Assef, R. J., Stern, D., Kochanek, C. S., et al. 2013, *ApJ*, 772, 26
- Banerji, M., McMahon, R. G., Hewett, P. C., et al. 2012, *MNRAS*, 427, 2275
- Becker, R. H., White, R. L., Gregg, M. D., et al. 2001, *ApJS*, 135, 227
- Benn, C. R., Vigotti, M., Carballo, R., Gonzalez-Serrano, J. I., & Sánchez, S. F. 1998, *MNRAS*, 295, 451
- Bennert, V. N., Treu, T., Woo, J.-H., et al. 2010, *ApJ*, 708, 1507
- Bentz, M. C., Peterson, B. M., Pogge, R. W., & Vestergaard, M. 2009, *ApJ*, 694, L166
- Borison, T. A., & Green, R. F. 1992, *ApJS*, 80, 109
- Bouchet, P., Lequeux, J., Maurice, E., Prevot, L., & Prevot-Burnichon, M. L. 1985, *A&A*, 149, 330
- Brotherton, M. S., Tran, H. D., Becker, R. H., et al. 2001, *ApJ*, 546, 775
- Calzetti, D., Kinney, A. L., & Storchi-Bergmann, T. 1994, *ApJ*, 429, 582
- Canalizo, G., Wold, M., Hiner, K. D., et al. 2012, *ApJ*, 760, 38
- Chambers, K. C., Magnier, E. A., Metcalfe, N., et al. 2016, *arXiv:1612.05560*
- Comastri, A., Fiore, F., Vignali, C., et al. 2001, *MNRAS*, 327, 781
- Cooke, A., & Rodgers, B. 2005, *Astronomical Data Analysis Software and Systems XIV*, 347, 514
- Croom, S. M., Smith, R. J., Boyle, B. J., et al. 2004, *MNRAS*, 349, 1397
- Cushing, M. C., Vacca, W. D., & Rayner, J. T. 2004, *PASP*, 116, 362
- Cutri, R. M., Nelson, B. O., Kirkpatrick, J. D., Huchra, J. P., & Smith, P. S. 2001, *The New Era of Wide Field Astronomy*, 232, 78
- Cutri, R. M., Nelson, B. O., Francis, P. J., & Smith, P. S. 2002, *IAU Colloq. 184: AGN Surveys*, 284, 127
- Elias, J. H., Joyce, R. R., Liang, M., et al. 2006, *Proc. SPIE*, 6269, 62694C
- Enya, K., Yoshii, Y., Kobayashi, Y., et al. 2002, *ApJS*, 141, 45
- Ferrarese, L., & Merritt, D. 2000, *ApJ*, 539, L9
- Fitzpatrick, E. L. 1999, *PASP*, 111, 63
- Fynbo, J. P. U., Krogager, J.-K., Venemans, B., et al. 2013, *ApJS*, 204, 6
- Gebhardt, K., Bender, R., Bower, G., et al. 2000, *ApJ*, 539, L13
- Georgakakis, A., Clements, D. L., Bendo, G., et al. 2009, *MNRAS*, 394, 533
- Georgakakis, A., Grossi, M., Afonso, J., & Hopkins, A. M. 2012, *MNRAS*, 421, 2223
- Glikman, E., Helfand, D. J., & White, R. L. 2006, *ApJ*, 640, 579
- Glikman, E., Helfand, D. J., White, R. L., et al. 2007, *ApJ*, 667, 673
- Glikman, E., Urrutia, T., Lacy, M., et al. 2012, *ApJ*, 757, 51

TABLE 8
BH MASSES, BOLOMETRIC LUMINOSITIES, AND λ_{Edd} VALUES OF NIR-RED AGNs

Object Name	$P\beta$			$P\alpha$		
	$\log M_{\text{BH}}$ (M_{\odot})	$\log L_{\text{bol}}$ (erg s^{-1})	λ_{Edd}	$\log M_{\text{BH}}$ (M_{\odot})	$\log L_{\text{bol}}$ (erg s^{-1})	λ_{Edd}
0106+2603	—	—	—	—	—	—
0157+1712	7.955±0.030	46.12±0.02	1.156±0.104	—	—	—
0221+1327	7.686±0.035	45.31±0.03	0.336±0.037	7.567±0.018	45.01±0.02	0.222±0.013
0234+2438	—	—	—	—	—	—
0324+1748	8.381±0.012	46.67±0.01	1.551±0.052	—	—	—
0348+1255	—	—	—	—	—	—
1258+2329	7.354±0.117	45.45±0.05	0.999±0.333	7.675±0.032	45.38±0.03	0.403±0.044
1307+2338	—	—	—	—	—	—
1453+1353	—	—	—	7.420±0.048	44.73±0.04	0.162±0.026
1543+1937	8.337±0.092	45.93±0.04	0.308±0.079	8.266±0.021	45.94±0.02	0.376±0.026
1659+1834	8.939±0.012	45.80±0.01	0.057±0.002	8.836±0.027	45.65±0.02	0.052±0.004
2222+1952	—	—	—	—	—	—
2222+1959	8.884±0.009	45.88±0.01	0.079±0.002	—	—	—
2303+1624	—	—	—	—	—	—
2327+1624	—	45.30±0.09	—	—	—	—
2344+1221	8.553±0.011	45.86±0.01	0.160±0.005	—	—	—

NOTE. — The listed properties of NIR-red AGNs are measured after correcting for the dust extinction by using the $E(B - V)_{\text{line}}$ values.

- Glikman, E., Simmons, B., Mailly, M., et al. 2015, arXiv:1504.02111
- Graham, A. W., Erwin, P., Caon, N., & Trujillo, I. 2001, ApJ, 563, L11
- Graham, A. W., & Driver, S. P. 2007, ApJ, 655, 77
- Grazian, A., Cristiani, S., D’Odorico, V., Omizzolo, A., & Pizzella, A. 2000, AJ, 119, 2540
- Greene, J. E., & Ho, L. C. 2005, ApJ, 630, 122
- Greene, J. E., Peng, C. Y., & Ludwig, R. R. 2010, ApJ, 709, 937
- Gregg, M. D., Becker, R. H., White, R. L., et al. 1996, AJ, 112, 407
- Gültekin, K., Richstone, D. O., Gebhardt, K., et al. 2009, ApJ, 698, 198
- Hopkins, P. F., Hernquist, L., Cox, T. J., et al. 2005, ApJ, 630, 705
- Hopkins, P. F., Hernquist, L., Cox, T. J., et al. 2006, ApJS, 163, 1
- Hopkins, P. F., Hernquist, L., Cox, T. J., & Keres, D. 2008, ApJS, 175, 356
- Im, M., Griffiths, R. E., & Ratnatunga, K. U. 1997, ApJ, 475, 457
- Im, M., Lee, I., Cho, Y., et al. 2007, ApJ, 664, 64
- Imanishi, M., Ichikawa, K., Takeuchi, T., et al. 2011, PASJ, 63, 447
- Jiang, Y.-F., Greene, J. E., & Ho, L. C. 2011, ApJ, 737, L45
- Jun, H. D., Im, M., Lee, H. M., et al. 2015, ApJ, 806, 109
- Kang, W.-R., Woo, J.-H., Schulze, A., et al. 2013, ApJ, 767, 26
- Kim, M., Ho, L. C., & Im, M. 2006, ApJ, 642, 702
- Kim, D., Im, M., & Kim, M. 2010, ApJ, 724, 386
- Kim, J. H., Im, M., Lee, H. M., et al. 2012, ApJ, 760, 120
- Kim, D., Im, M., Kim, J. H., et al. 2015, ApJS, 216, 17
- Kim, D., Im, M., Glikman, E., Woo, J.-H., & Urrutia, T. 2015, ApJ, 812, 66
- Kim, D., & Im, M. 2018, A&A, 610, A31
- Kocevski, D. D., Faber, S. M., Mozena, M., et al. 2012, ApJ, 744, 148
- Lacy, M., Ridgway, S. E., Gates, E. L., et al. 2013, ApJS, 208, 24
- Landt, H., Bentz, M. C., Ward, M. J., et al. 2008, ApJS, 174, 282
- Landt, H., Bentz, M. C., Peterson, B. M., et al. 2011, MNRAS, 413, L106
- Landt, H., Elvis, M., Ward, M. J., et al. 2011, MNRAS, 414, 218
- Lawrence, A., Warren, S. J., Almaini, O., et al. 2007, MNRAS, 379, 1599
- Lee, I., Im, M., Kim, M., et al. 2008, ApJS, 175, 116
- Lusso, E., Comastri, A., Simmons, B. D., et al. 2012, MNRAS, 425, 623
- Lynden-Bell, D. 1969, Nature, 223, 690
- Kobayashi, N., Tokunaga, A. T., Terada, H., et al. 2000, Proc. SPIE, 4008, 1056
- Maddox, N., & Hewett, P. C. 2006, MNRAS, 367, 717
- Marble, A. R., Hines, D. C., Schmidt, G. D., et al. 2003, ApJ, 590, 707
- Magorrian, J., Tremaine, S., Richstone, D., et al. 1998, AJ, 115, 2285
- Markwardt, C. B. 2009, Astronomical Data Analysis Software and Systems XVIII, 411, 251
- Massey, P., Strobel, K., Barnes, J. V., & Anderson, E. 1988, ApJ, 328, 315
- McLure, R. J., & Dunlop, J. S. 2004, MNRAS, 352, 1390
- Park, D., Woo, J.-H., Bennert, V. N., et al. 2015, ApJ, 799, 164
- Polletta, M., Weedman, D., Hönig, S., et al. 2008, ApJ, 675, 960-984
- Puchnarewicz, E. M., & Mason, K. O. 1998, MNRAS, 293, 243
- Rayner, J. T., Toomey, D. W., Onaka, P. M., et al. 2003, PASP, 115, 362
- Risaliti, G., & Elvis, M. 2005, ApJ, 629, L17
- Rose, M., Tadhunter, C. N., Holt, J., & Rodríguez Zaurín, J. 2013, MNRAS, 432, 2150
- Sanders, D. B., Soifer, B. T., Elias, J. H., et al. 1988, ApJ, 325, 74
- Sanders, D. B., & Mirabel, I. F. 1996, ARA&A, 34, 749
- Schawinski, K., Treister, E., Urry, C. M., et al. 2011, ApJ, 727, L31
- Schawinski, K., Simmons, B. D., Urry, C. M., Treister, E., & Glikman, E. 2012, MNRAS, 425, L61
- Schlafly, E. F., & Finkbeiner, D. P. 2011, ApJ, 737, 103
- Schneider, D. P., Hall, P. B., Richards, G. T., et al. 2005, AJ, 130, 367
- Sheinis, A. I., Bolte, M., Epps, H. W., et al. 2002, PASP, 114, 851
- Shen, Y., Richards, G. T., Strauss, M. A., et al. 2011, ApJS, 194, 45
- Shen, Y., Greene, J. E., Ho, L. C., et al. 2015, ApJ, 805, 96
- Simmons, B. D., Urry, C. M., Schawinski, K., Cardamone, C., & Glikman, E. 2012, ApJ, 761, 75
- Skrutskie, M. F., Cutri, R. M., Stiening, R., et al. 2006, AJ, 131, 1163
- Smith, P. S., Schmidt, G. D., Hines, D. C., Cutri, R. M., & Nelson, B. O. 2002, ApJ, 569, 23
- Stern, D., Assef, R. J., Benford, D. J., et al. 2012, ApJ, 753, 30
- Suh, H., Hasinger, G., Steinhardt, C., Silverman, J. D., & Schramm, M. 2015, ApJ, 815, 129
- Tokunaga, A. T., Kobayashi, N., Bell, J., et al. 1998, Proc. SPIE, 3354, 512
- Tozzi, P., Gilli, R., Mainieri, V., et al. 2006, A&A, 451, 457
- Tremaine, S., Gebhardt, K., Bender, R., et al. 2002, ApJ, 574, 740
- Urrutia, T., Lacy, M., & Becker, R. H. 2008, ApJ, 674, 80-96
- Urrutia, T., Becker, R. H., White, R. L., et al. 2009, ApJ, 698, 1095
- Urrutia, T., Lacy, M., Spoon, H., et al. 2012, ApJ, 757, 125
- Vacca, W. D., Cushing, M. C., & Rayner, J. T. 2003, PASP, 115, 389
- Vanden Berk, D. E., Richards, G. T., Bauer, A., et al. 2001, AJ, 122, 549

- Véron-Cetty, M.-P., & Véron, P. 2006, *A&A*, 455, 773
- Webster, R. L., Francis, P. J., Petersont, B. A., Drinkwater, M. J., & Masci, F. J. 1995, *Nature*, 375, 469
- Whiting, M. T., Webster, R. L., & Francis, P. J. 2001, *MNRAS*, 323, 718
- Wilkes, B. J., Schmidt, G. D., Cutri, R. M., et al. 2002, *ApJ*, 564, L65
- Woo, J.-H., & Urry, C. M. 2002, *ApJ*, 579, 530
- Woo, J.-H., Treu, T., Malkan, M. A., & Blandford, R. D. 2006, *ApJ*, 645, 900
- Woo, J.-H., Treu, T., Malkan, M. A., & Blandford, R. D. 2008, *ApJ*, 681, 925-930
- Woo, J.-H., Treu, T., Barth, A. J., et al. 2010, *ApJ*, 716, 269
- Woo, J.-H., Yoon, Y., Park, S., Park, D., & Kim, S. C. 2015, *ApJ*, 801, 38
- Wright, E. L., Eisenhardt, P. R. M., Mainzer, A. K., et al. 2010, *AJ*, 140, 1868
- Young, M., Elvis, M., & Risaliti, G. 2009, *ApJS*, 183, 17